Journal of Vibration Engineering & Technologies (2025)13:257
https://doi.org/10.1007/s42417-025-01799-5

ORIGINAL PAPER

Electromechanical Modelling and Chaotic Vibration Analysis of a Coupled Hydroturbine-Generator Set by Considering Multiple Effects and Forces

Ehsan Masalegoo[1] · Ali Soleimani[1] · Mohammad Farrokhpour[1]

Received: 5 September 2024 / Revised: 5 February 2025 / Accepted: 26 February 2025

Abstract

Purpose Understanding and analyzing the vibrations of a hydroturbine-generator set is necessary for its optimal design. Vibration analysis can also be very useful for implementing maintenance procedures. To obtain useful results from vibration analysis, system modeling is also of particular importance. In this paper, the hydroturbine-generator set is modeled as a couple and various effects such as gyroscopic, arcuate whirl and etc. are considered.

Methods A new electromechanical model for the lateral-torsional vibration of a coupled hydroturbine-generator considering is developed. The gyroscopic effect, unbalanced magnetic pull, arcuate whirl, oil film force and seal force are considered in the new mathematical modelling. In the electromechanical model, the equations of the generator and hydroturbine vibration are coupled and should be solved together. The Runge–Kutta numerical method is used to solve governing equations at different rotational speeds and vibration responses are obtained in lateral and torsional directions for hydroturbine and generator rotors. Vibration responses are analyzed through time signal, frequency spectrum, phase plane and Poincare section.

Results Result show chaotic behavior in the lateral and torsional vibrations of the hydroturbine and generator rotors. Time signals show periodic behaviors but not exactly repeated. Many and varied combinations of frequencies are observed in the frequency spectrum. Also, the phase planes illustrated chaotic vibrations with different strange attractors. New structured geometries obtained in the Poincare sections which in not reported earlier. The results can be used for the design of hydroturbine-generator set and to monitoring the system condition.

Keywords Chaos · Generator · Hydroturbine · Vibration · Phase plane · Spectrum · Frequency

List of symbols

x1	Lateral displacement of generator in the x direction
x2	Lateral displacement of hydroturbine in the x direction
y1	Lateral displacement of generator in the y direction
y2	Lateral displacement of hydroturbine in the y direction
θ	Rotation angle of hydroturbine-generator set
m_1	Mass of the generator rotor
m_2	Mass of the hydroturbine runner
k_1	Upper bearing stiffness of the generator rotor
k_2	Lower bearing stiffness of the generator rotor
k_3	Bearing stiffness of the hydroturbine
c_1	Damping coefficient of the generator rotor bearings
c_2	Damping coefficient of the hydroturbine runner bearings
c_3	Structural damping coefficient of the generator rotor
e_1	Mass eccentricity of the generator rotor
e_2	Mass eccentricity of the hydroturbine runner
J_1	Inertia of the generator rotor
J_2	Inertia of the hydroturbine runner
J_p	Inertia of the generator rotor about the axis of rotation
J_d	Inertia of the generator rotor about the axis diameter
δ	Spring constant of the generator shaft against force F
μ	Spring constant of the generator shaft against moment M
a	Center distance of the upper bearing and generator rotor

✉ Ali Soleimani
soleimani@iau.ac.ir

[1] Department of Mechanical Engineering, Najafabad Branch, Islamic Azad University, Najafabad, Iran

Published online: 09 April 2025

b	Center distance of the generator rotor and lower bearing
c	Center distance of the lower bearing and turbine support
d	Center distance of the turbine support and hydroturbine runner
k_r	Radial stiffness of the stator
f	Friction coefficient between rotor and stator
μ_b	Viscosity coefficient of bearing oil
c_z	Radial clearance between shaft and bearing
L_b	Journal bearing length
R_b	Radius of the journal bearing
L_s	Length of the labyrinth seal
R_s	Radius of the labyrinth seal
v	Linear flow velocity in the seal
ν	Hydrodynamic viscosity coefficient
ΔP	Labyrinth seal pressure
L_g	Length of the generator rotor
R_g	Radius of the generator rotor
μ_0	Magnetic permeability coefficient
I_j	Excitation current
δ_0	Air gap clearance between rotor and stator
k_j	Magnetic resistivity coefficient

Introduction

As a renewable energy source with minimal environmental impact, low operational costs, and widespread usage, electricity is suitable and can largely meet energy demand. Currently, hydropower plants provide approximately 30% of the world's electrical energy production [1]. Due to climate change, the use and development of hydroelectric power plants have garnered widespread attention in countries with abundant water resources. Consequently, the safe and stable operation of hydroelectric power plants is increasingly important in engineering and is directly related to improving electricity production quality and optimizing the power grid. The hydroturbine generator set is one of the main components of hydroelectric power plants.

With the increasing demand and capacity for electricity production, there have been increased vibration problems in the hydroturbine generator set. Excessive vibrations not only affect the safety and efficiency of hydroelectric power plants but also increase the likelihood of accidents. Therefore, examining the vibrations and dynamic behaviors of the hydroturbine-generator set is of particular importance for implementing more precise protective measures and ensuring the optimal performance of the power plant.

In rotating machinery, due to various factors such as mass imbalance and others, mechanical vibrations are an inevitable phenomenon and are always present. Excessive vibrations are often accompanied by severe dynamic loads, which can cause component failures and disrupt system performance, sometimes resulting in significant costs. On the other hand, processing and analyzing vibration signals can help determine the machine's condition and health and assist in system fault diagnosis. For this reason, conducting precise analyses in the field of vibrations in rotating machinery is essential.

The issue of vibrations in the hydroturbine-generator set is significantly different from that in other rotating machinery. For a more precise vibration analysis of the hydroturbine-generator set, it is necessary to consider the impact of the hydrodynamic pressure of fluid flow, electromagnetic forces, the structure of the turbine and generator, and various complex forces, including arcuate whirl and gyroscopic effects, in the modeling.

The modelling of hydroturbine to study its vibration are done by several researchers. Awad et al. [2] assessed the primary role of the turbine inlet valve (TIV) in a hydroelectric power plant. They introduced a simplified theoretical model that explains the mechanism behind periodic seal vibrations and simulates the plant's transient response. A hydropower conversion system based on vortex-induced vibrations is investigated experimentally [3]. To conduct an acceptable analysis of the system, thorough and accurate modeling is required to derive its governing equations. This facilitates the examination and analysis of frequency response, time-domain plots, phase planes, Poincaré maps, chaos, and more [4–6].

For accurate modelling of the hydroturbine-generator set, there are important forces and effects which are studied in references. Perez-Loya et al. [7] studied electromagnetic losses in synchronous machines during unbalancing due to magnetic pull. They investigate fluid–solid interactions with the impact of hydrodynamic damping during resonance and rotor–stator interactions, and the importance of damping in preventing damage to hydroturbines. Trivedi [8] reviewed fluid–solid interactions in hydroturbines.

Giannini [9] utilized a numerical method for examining flutter instability in stable dynamic systems while considering the gyroscopic effect was presented. Zeng et al. [10] studied the impact of the gyroscopic phenomenon on the stability of linear and nonlinear critical speeds. They used a 20-degree-of-freedom model consisting of a rotor system and two disks, considering gyroscopic effects. Ma et al. [11] examined the impact of the imbalance of the two disks on the stability of the system and the nonlinear responses of the bearing and rotor. Zhang et al. [12] investigate the

nonlinear dynamic characteristics of a bearing-rotor system, considering slip and impact between the rotor and stator for the hydroturbine-generator set. Patel et al. [13] analyzed the nonlinear lateral-torsional vibrations of the rotor in contact with the stator via bifurcation diagrams. Li et al. [14] examined and studied the dynamic behavior of a hydroturbine-generator set considering the linear oil film force of the bearings and the magnetic attractive force under the gyroscopic effect. Shi et al. [15] focused on mathematical modeling to analyze coupled torsional and lateral vibrations in the hydroturbine-generator set, considering only arcuate whirl.

As a result of vibration analysis in hydroturbine-generator set, condition monitoring and fault detection are illustrated in some research papers. Kong et al. [16] studied the complex and non-linear connection between vibration behavior and fault types in hydropower units (HU), and introduced a fault diagnosis model. Their model, utilizing a hybrid feature vector set and an optimized Extreme Learning Machine (ELM), aims to enhance the differentiation of various vibration faults in HU, building upon existing diagnostic techniques. Masalegoo et al. [17] introduced a novel method for diagnosing primary faults in electrical motors and gearboxes, utilizing recurrence quantitative analysis and recurrence plots. Their findings revealed that features derived from chaotic behavior could efficiently assess vibration signals from rotating machinery, enabling accurate fault diagnosis with minimal error. Soleimani et al. [18] proposed an early fault detection method for bearings and gearboxes by extracting chaotic features from experimental vibration data. Their experimental results indicated that this approach could identify abnormalities in gears and bearings, while accurately determining fault types. Feng et al. [19] demonstrated that cavitation reduces Kaplan turbine efficiency and causes vibrations, but detecting it remains challenging. Their study employs a high-speed camera and a vibration monitoring system on a hydraulic test platform, revealing multifractal characteristics in the vibration signals. Their findings propose an effective method for identifying cavitation in Kaplan turbines.

Hydroturbine and generator are affected by together, so that coupled modelling has more efficiency. Xu et al. [20] developed a coupled model of the generator and hydroturbine system and studied the impact of misalignment in the coupling on the vibrations of the rotating machinery. Song et al. [21] examined the characteristics of the torsional vibrations of the hydroturbine-generator set. They considered the effects of fluid hydraulic forces and electromagnetic forces. Also, the frequency spectra of the shaft torque, phase diagrams, and electromagnetic torque are presented. Xu et al. [22], presented a mathematical model with six fractional orders considering the damping force, oil film force, asymmetric magnetic pull, and asymmetric hydraulic force. They studied the nonlinear dynamics of the generator-hydroturbine set were examined via six fractional orders. Shi et al. [23] conducted stability and sensitivity analyses of parameters related to governor control in the hydroturbine-generator set, and studied the optimal controller design for stable performance. Zhuang et al. [24] investigated the vibrational characteristics and dynamic behaviors via a turbulent fluid flow model that considers hydraulic forces on asymmetric turbine blades in a hydroturbine-generator set. Their study finds that an increased Reynolds number can intensify these vibrations, leading to complex nonlinear bifurcations and chaotic motion. Sun et al. [25] performed nonlinear mathematical modeling of the hydroturbine-generator set considering the dynamic properties of the structure and the foundation of the installation site, the oil film force within the bearings, and the water sealing force. Additionally, the vibration response of the system is investigated and studied. Li et al. [26] highlighted that hydraulic excitation in a hydro-turbine generator unit exhibits clear non-stationary behavior. To address this, their study examined the reliability of non-stationary random vibrations in such units. Their findings provide an effective solution to the challenges associated with the non-stationary random vibration reliability of Francis hydro-turbine generator units. Wang et al. [27] conducted a predictive analysis method of shafting vibration for the hydraulic turbine generator unit. Hydraulic vibrations play a crucial role in influencing the stability and performance of hydro-turbine generator units (HGUs). Zhuang et al. [28] examines the nonlinear dynamic behavior of HGUs caused by hydraulic vibrations. The study reveals that a rise in the Reynolds number intensifies these vibrations, potentially resulting in more intricate nonlinear bifurcations and chaotic dynamics.

Such investigations can assist in measuring mechanical vibrations, identifying new dynamic behaviors, and advancing fault diagnosis methods in real-world systems. They also provide deeper insights into the system's health. Additionally, when designing new systems, these analyses can be applied to create optimal operating conditions that ensure better dynamic behavior and acceptable vibration levels, ultimately improving efficiency and performance.

In this work, dynamic modeling of the hydroturbine and generator assembly with variable rotational speeds, considering gyroscopic effects, mass imbalance along with arcuate whirl due to centrifugal forces in the generator, hydroturbine, and bearings, was carried out. Moreover, the simultaneous impacts of nonlinear forces from the seal and oil film of the bearing, the magnetic pull force of the generator, and friction and impact forces during rotor–stator contact in the generator are included in this modeling.

Previous studies have not performed dynamic modeling of hydroturbine-generator assemblies in this manner. Additionally, lateral vibration analysis of the generator rotor and the hydroturbine driver was performed via phase plane diagrams and Poincare maps, and various effects considered in the modeling were examined.

New dynamic behaviors and vibrational phenomena have been observed in the results, which can be utilized in analyzing measured vibrations in real systems. These results can also aid in methods for preventing generator and turbine failures, reducing machine efficiency during electricity production, and preventing downtime. The distinctive feature and innovations of this research, compared with those of previous studies, lie in the proposed model and analysis methods.

The results of this research can be used in the design of hydroturbines as well as in their maintenance and operation. These improvements are important and effective in the production of electrical energy by hydroturbines. Hydroturbines work with water, which is a clean source of energy, and for this reason there is great interest in the world for the production and use of this sustainable energy. One of the sutainable development golas is to "ensure access to affordable, reliable, sustainable and modern energy for all". If hydropower generation well-planned and implemented, it has play significant role in achieving sustainable development goals.

Materials and Methods

The sheme of hydroelectric power plant systems is depicted in Fig. 1. These systems mainly consist of a dam, a secondary reservoir to control sudden changes in water pressure, diversion tunnels, water intake channels, hydroelectric turbines, generators, and the location for discharging water behind the dam. Among these components, the hydroelectric turbine-generator set is one of the main pieces of equipment used for electricity generation, with the aim of converting mechanical energy into electrical energy. Therefore, the structure and performance of the hydroelectric turbine-generator set play a fundamental role in the operation, stability, and efficiency improvement of power plants.

A hydroelectric turbine is a rotating machine that converts the potential energy of water into mechanical energy. The amount of energy produced depends on parameters such as the head, flow rate, and losses. Hydroelectric turbines are usually divided into three main categories: Pelton wheels, Francis turbines, and Kaplan turbines, with the choice of turbine depending on the head and flow rate of water. Vertical Francis turbines are commonly used in many large- and medium-sized power plants. The generator is the most important component of a hydroelectric power plant; it converts rotational mechanical energy into electrical energy and consists of two main parts: the rotor and the stator.

In reality, vibrations caused by the gyroscopic effect exist in all similar rotating machines, and the hydroturbine-generator set is no exception to this rule. The generator rotor not only undergoes horizontal displacement but also

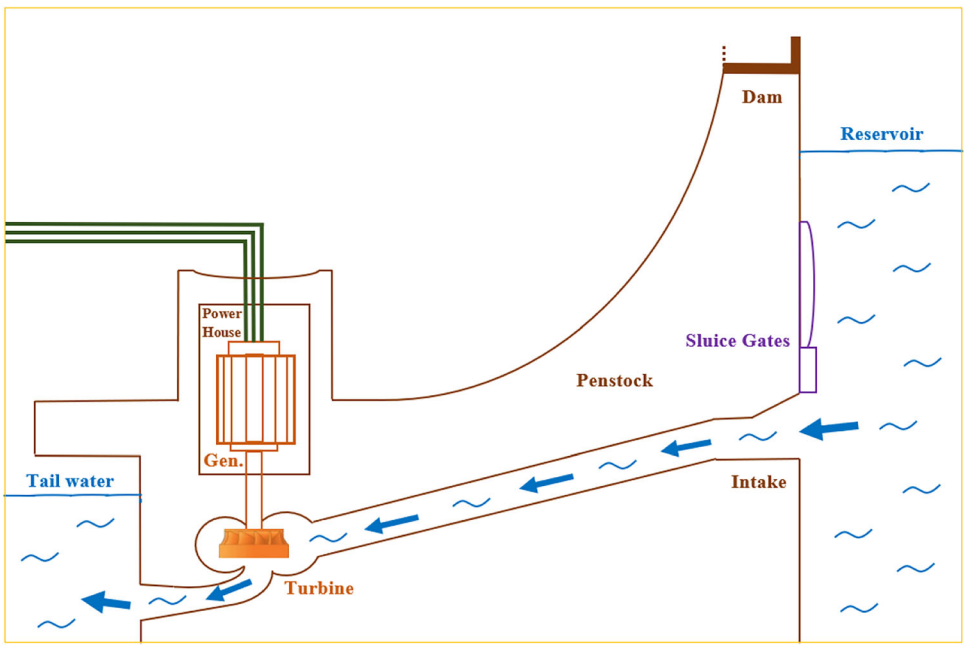

Fig. 1 Scheme of a hydroelectric power plant

experiences vertical displacement (angular rotation) during arcuate whirl. Currently, with the rapid growth in demand for electricity generation, hydroturbine-generator units are trending toward high capacities, speeds, and power outputs, which exacerbates vibration issues in the hydroturbine-generator set. Specifically, the gyroscopic effect is one of the causes of vibration, and therefore its effects cannot be ignored in the analysis of vibrations in hydroelectric power plants.

In this work, in addition to lateral vibrations, torsional vibrations are investigated. Torsional vibrations mainly occur due to the loss of rotational torque balance between the generator rotor and the hydroturbine axis in the hydroturbine-generator set. During rotation, the movement of water flow creates torque on the hydroturbine impeller, and on the other hand, electromagnetic torque is exerted on the generator rotor due to random disturbances in the flow and changes in status, which leads to phase differences and torsional vibrations.

Additionally, various factors, such as irregularities in the input water flow to the hydroturbine and mechanical torques, also exist, which create different aspects of torsional axis vibration. Generally, the hydroturbine-generator set is an electromechanically coupled rotating machine whose dynamic behavior is influenced by electromagnetic forces; therefore, it is associated mainly with lateral-torsional vibrations, which can significantly affect the system's performance. Hence, in this work, considering the vibration-causing factors mentioned in the previous section, the dynamic behavior of a hydroturbine-generator set with lateral and torsional vibrations is modeled.

Modeling the Coupled Lateral-Torsional Vibrations of the Hydroelectric Turbine-Generator Set

The structure and components of the rotating axis in the hydroturbine-generator set are illustrated in Fig. 2a. O_1 and O_2 represent the geometric centers of the generator rotor and the hydroturbine runner, respectively, and C_1, C_2, and C_3 represent the geometric centers of the upper bearing, lower bearing, and hydroturbine bearing, respectively. r_1 to r_5 represent the radii of arcuate whirl for the generator, hydroturbine impeller, upper and lower generator bearings, and hydroturbine bearing during vibration, whose mathematical relationships are derived as Eq. (1).

$$\begin{cases} |O_1C_1| = a \\ |O_1C_2| = b \\ |C_2C_3| = c \\ |O_2C_3| = d \end{cases} \tag{1}$$

From the geometry of Fig. 2a, Eqs. (2) to (6) can be obtained.

$$r_1 = \sqrt{(x_1^2 + y_1^2)} \tag{2}$$

$$r_2 = \sqrt{(x_2^2 + y_2^2)} \tag{3}$$

$$r_3 = \frac{[(a+b)(b+c+d) - a(c+d)]r_1 + abr_2}{b(b+c+d)} \tag{4}$$

$$r_4 = \frac{(c+d)r_1 + br_2}{b+c+d} \tag{5}$$

$$r_5 = \frac{dr_1 + (b+c)r_2}{b+c+d} \tag{6}$$

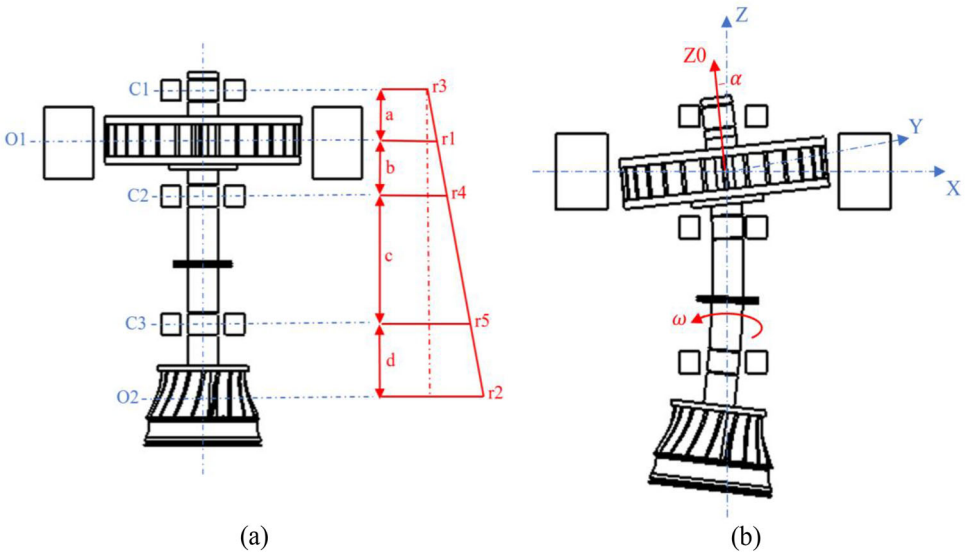

Fig. 2 Rotor of the hydroturbine-generator set: **a** undeformed, **b** deformed

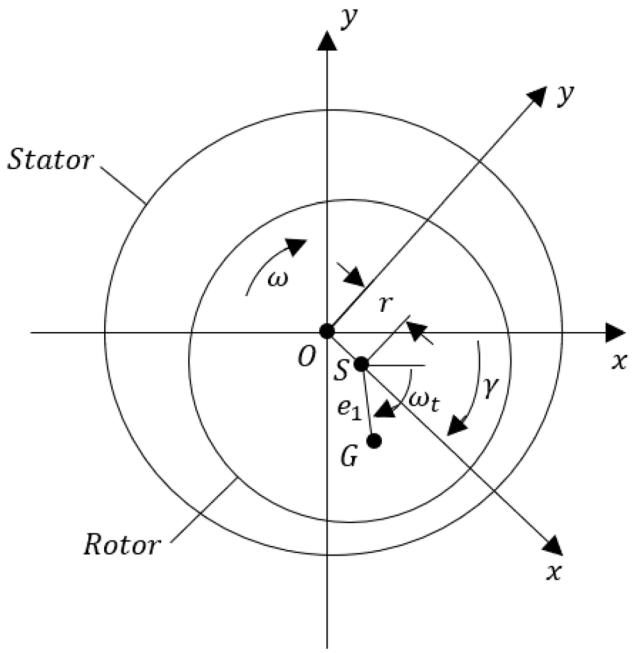

Fig. 3 Eccentric rotor

Figure 3 represents the rotor eccentricity. In the Cartesian coordinate system xyz, points O, G, and S denote the geometric center of the stator, the center of mass of the rotor, and the geometric center of the rotor, respectively. The distance between center of mass and center of rotation is indicates by e_1. r is the radius of rotation of the geometric center of the rotor about the geometric center of the stator. When the rotor is stationary, point O coincides with point S. In real hydroturbine-generator sets, the distances between the generator rotor and the bearings at the top and bottom are generally not equal. This causes point S to not only have a centrifugal force away from the center F but also to have a torque M [24].

Figure 2b depicts the angle α, which represents the deviation of the rotor rotation axis due to gyroscopic effects relative to the principal axis. The rotor deviation angle can be expressed via Euler angles in different directions. The parameters α, β, and γ are used in this work to represent the Euler angles, indicating the precession angle, deflection angle, and rotation angle, respectively, and their range of variation can be observed according to Eq. (7).

$$\begin{cases} 0 \le \gamma \le 2\pi \\ 0 \le \beta \le 2\pi \\ 0 \le \alpha \le \pi \end{cases} \tag{7}$$

Kinetic Energy

The Euler angles for point S are decomposed into components S_{x0}, S_{y0}, and S_{z0}, and the angular velocity ω around each axis is written as Eq. (8) [23].

$$\begin{cases} \omega_1 = \omega_x = \dot{\beta}\sin\alpha\sin\gamma + \dot{\alpha}\cos\gamma \\ \omega_2 = \omega_y = \dot{\beta}\sin\alpha\cos\gamma - \dot{\alpha}\sin\gamma \\ \omega_3 = \omega_z = \dot{\beta}\cos\alpha + \dot{\gamma} \end{cases} \tag{8}$$

On the basis of above, the equation for the kinetic energy of a rigid body for the fixed-point S is written as Eq. (9), where J_d is the moment of inertia about the axes S_{x0} and S_{y0}, and J_p is the moment of inertia about the axis S_{z0}.

$$T_s = \frac{1}{2}\left[\left(\omega_x^2 + \omega_y^2\right)J_d + \omega_z^2 J_p\right] \tag{9}$$

m_1 and m_2 represent the masses of the generator rotor and turbine runner, respectively, and k_1, k_2, and k_3 represent the stiffness coefficients of the upper and lower bearings of the generator rotor and the turbine runner bearing, respectively. The coordinates of the generator rotor center and turbine runner center are (x_{01}, y_{01}) and (x_{02}, y_{02}), respectively, and e_1 and e_2 represent the mass eccentricites of the generator rotor and turbine runner, respectively.

Considering the lateral-torsional vibrations for the system, the rotation angles of the generator rotor φ_1 and the turbine runner φ_2 are considered. On this basis, considering the imbalance of the generator rotor and turbine runner, the Cartesian coordinates of the center of rotation are expressed as Eqs. (10) and (11).

$$\begin{cases} x_{01} = x_1 + e_1\cos\varphi_1 \\ y_{01} = y_1 + e_1\sin\varphi_1 \end{cases} \tag{10}$$

$$\begin{cases} x_{02} = x_2 + e_2\cos\varphi_2 \\ y_{02} = y_2 + e_2\sin\varphi_2 \end{cases} \tag{11}$$

As a result, the total kinetic energy equation of the system, considering lateral-torsional vibrations in the system modeling, is written according to Eq. (12).

$$\begin{aligned} T = {} & \frac{1}{2}m_1\left(\dot{x}_1^2 + \dot{y}_1^2 + e_1^2\dot{\varphi}_1^2 + 2e_1\dot{\varphi}_1\dot{y}_1\cos\varphi_1 - 2e_1\dot{\varphi}_1\dot{x}_1\sin\varphi_1\right) \\ & + \frac{1}{2}\left(J_1 + m_1e_1^2\right)\dot{\varphi}_1^2 \\ & + \frac{1}{2}m_2\left(\dot{x}_2^2 + \dot{y}_2^2 + e_2^2\dot{\varphi}_2^2 + 2e_2\dot{\varphi}_2\dot{y}_2\cos\varphi_2 - 2e_2\dot{\varphi}_2\dot{x}_2\sin\varphi_2\right) \\ & + \frac{1}{2}\left(J_2 + m_2e_2^2\right)\dot{\varphi}_2^2 \\ & + \frac{1}{2}\left[\left(\dot{\alpha}_x^2 + \dot{\alpha}_y^2\right)J_d + \left[\dot{\varphi}_1 + \dot{\varphi}_1\left(\dot{\alpha}_x\alpha_y - \alpha_x\dot{\alpha}_y\right)\right]J_p\right] \end{aligned} \tag{12}$$

The effect of gyroscopic forces on the generator rotor is considered in the equation of kinetic energy. Additionally, it is assumed that identical blades are used in the hydroturbine runner, spaced equally on the axis.

Potential Energy

With the consideration of vibrations arising from angular rotation, bending, and inclined vibration of the generator shaft, the potential energy is expressed as Eq. (13) [24].

$$\begin{aligned} U = {} & \left(x_1^2 + y_1^2\right)K_{11} + \left(x_2^2 + y_2^2\right)K_{22} \\ & + \sqrt{\left(x_1^2 + y_1^2\right)\left(x_2^2 + y_2^2\right)}K_{12} + \mu\alpha + \frac{1}{2}\delta\alpha^2 \\ & + \frac{1}{2}K_y(\varphi_1 - \varphi_2)^2 \end{aligned} \tag{13}$$

Here, K_y represents the torsional stiffness coefficient of the spindle, which is obtained from Eq. (14).

$$\begin{aligned} K_y &= \frac{E\pi\left(d_H^2 - d_B^2\right)}{32l} \\ l &\approx a + b + c + d \end{aligned} \tag{14}$$

In Eq. (14), E, d_H, d_B, and l represent the modulus of elasticity, inner diameter, outer diameter, and length of the spindle, respectively. Additionally, the length of the spindle is assumed to be approximately equal to the sum of the distances between components. In Eq. (13), μ denotes the spring constant of the generator rotor against the applied force F, and δ represents the spring constant of the generator rotor against the applied torque M. By disintegrating the deflection angle α in the x and y directions, Eq. (13) can be rewritten as Eq. (15) [15].

$$\begin{aligned} U = {} & K_{11}\left(x_1^2 + y_1^2\right) + K_{22}\left(x_2^2 + y_2^2\right) \\ & + K_{12}\sqrt{\left(x_1^2 + y_1^2\right)\left(x_2^2 + y_2^2\right)} + \mu\left(x_1\alpha_x + y_1\alpha_y\right) \\ & + \frac{\delta}{2}\left(\alpha_x^2 + \alpha_y^2\right) + \frac{1}{2}K_y(\varphi_1 - \varphi_2)^2 \end{aligned} \tag{15}$$

where K_{11}, K_{22}, and K_{12} represent the equivalent stiffness in the direction of lateral vibrations of the axis of the hydroturbine-generator set and are calculated according to Appendix (51) [14]. Additionally, k_1, k_2, and k_3 used in Appendix (51), represent the stiffnesses of the upper and lower generator bearings and the turbine bearing, respectively. Also, the coefficients A_1, A_2, and B used in Appendix (51) are obtained via Appendix (52).

Lagrange Equation

The Lagrange equation is written according to Eq. (16) using the potential energy and kinetic energy.

$$L = T - U \tag{16}$$

With the consideration of lateral-torsional vibrations, the chosen generalized coordinates are according to Eq. (17).

$$q_i = \{x_1, y_1, x_2, y_2, \alpha_x, \alpha_y, \varphi_1, \varphi_2\} \tag{17}$$

Indeed, according to Eq. (18), the Lagrange equation governing the system is obtained.

$$\frac{d}{dt}\left(\frac{\partial L}{\partial \dot{q}_i}\right) - \frac{\partial L}{\partial q_i} = \sum F_i, \quad i = 1, 2, \ldots, 8 \tag{18}$$

Notably, the presence of external forces such as an oil film inside the bearings, a mechanical seal, a magnetic pull, a centrifugal force due to arcuate whirl, impact-friction, and torques M_g and M_t have been considered in the modeling of lateral-torsional vibrations, as defined by Eq. (19).

$$\begin{aligned} \sum F_1 &= -c_1\dot{x}_1 + F_{x-ump} + F_{x-rub} + F_{GG}\cos\varphi_1 \\ \sum F_2 &= -c_1\dot{y}_1 + F_{y-ump} + F_{y-rub} + F_{GG}\sin\varphi_1 \\ \sum F_3 &= -c_2\dot{x}_2 + F_{x-oil} + F_{x-seal} + F_{GT}\cos\varphi_2 \\ \sum F_4 &= -c_2\dot{y}_2 + F_{y-oil} + F_{y-seal} + F_{GT}\sin\varphi_2 \\ \sum F_5 &= -c_3\dot{\alpha}_x \\ \sum F_6 &= -c_3\dot{\alpha}_y \\ \sum F_7 &= -M_g \\ \sum F_8 &= M_t \end{aligned} \tag{19}$$

The torques M_g and M_t, which represent the external torques applied to the generator rotor due to the magnetic field and to the turbine runner due to the water flow, respectively, are defined by Eq. (20).

$$\begin{cases} M_g = \dfrac{P_g}{\dot{\varphi}_1} \\ M_t = \dfrac{P_t}{\dot{\varphi}_2} \end{cases} \tag{20}$$

where P_g, P_t, $\dot{\varphi}_1$, and $\dot{\varphi}_2$ represent the output power of the generator, the output power of the turbine, the rotational speed of the generator rotor, and the rotational speed of the turbine runner, respectively. c_1, c_2, and c_3 are the damping coefficients of the generator rotor and turbine runner in the x and y directions, and the damping coefficient of the rotor during bending and deflection due to the gyroscopic effect.

$F_{x\text{-ump}}$ and $F_{y\text{-ump}}$ represent the imbalance forces exerted by the magnetic pull on the generator rotor in the x and y directions, $F_{x\text{-rub}}$ and $F_{y\text{-rub}}$ represent the impact and friction forces occurring when the rotor collides with the stator during rotation, $F_{x\text{-oil}}$ and $F_{y\text{-oil}}$ represent the nonlinear forces due to the oil film in the turbine bearings in the x and y directions, $F_{x\text{-seal}}$ and $F_{y\text{-seal}}$ represent the nonlinear forces due to the water seal or turbine casing resulting from hydrodynamic fluid in the x and y directions, and finally, F_{GG} and F_{GT} represent the forces generated owing to the rotation of the generator and turbine runner, respectively.

The Unbalanced Force Due to Magnetic Pull

The unbalanced forces due to the magnetic pull are presented by Wu et al. [29] and obtained from Eq. (21).

$$\begin{cases} F_{x-ump} = \dfrac{R_g L_g \pi k_j^2 I_j^2}{4\mu_0}(2\Lambda_0\Lambda_1 + \Lambda_1\Lambda_2 + \Lambda_2\Lambda_3)\cos\varphi_1 \\ F_{y-ump} = \dfrac{R_g L_g \pi k_j^2 I_j^2}{4\mu_0}(2\Lambda_0\Lambda_1 + \Lambda_1\Lambda_2 + \Lambda_2\Lambda_3)\sin\varphi_1 \end{cases} \tag{21}$$

where R_g, L_g, δ_0, φ_1, e, ε, μ_0, I_j, and k_j represent the radius of the generator rotor, the length of the generator rotor, the air gap distance between the rotor and stator, the rotation angle of the hydroturbine runner, the radial displacement of the generator rotor, the eccentricity ratio of the rotor, the magnetic permeability coefficient, the excitation current of the generator, and the magnetic resistance coefficient, respectively. The radial displacement of the generator rotor is obtained via Eq. (22) and the eccentricity ratio is obtained via Eq. (23). Λ_0, Λ_1, Λ_2, and Λ_3 used in Eq. (21) are four intermediate variables without physical interpretation and are obtained from Appendix (53).

$$e = \sqrt{x_1^2 + y_1^2} \tag{22}$$

$$\varepsilon = \frac{e}{\delta_0} \tag{23}$$

The Rub-Impact Force Between the Rotor and Stator

The assumption is that there is an initial distance δ_0 between the stator and rotor. During one complete rotation, the time of contact is so short that the radial force resulting from the contact between the stator and rotor can be considered elastic; similarly, the tangential force during rubbing can be considered frictional force [30]. The radial force F_n and the tangential force F_t can be written as Eq. (24), where f and k_t are the coefficients of friction between the stator and rotor and the radial stiffness of the stator, respectively. In the xy coordinate system, these two forces can be rewritten as Eq. (25).

$$\begin{cases} F_n = (e-\delta_0)k_r, (e \geq \delta_0) \\ F_t = f \times F_n \end{cases} \tag{24}$$

$$\begin{bmatrix} F_{x-rub} \\ F_{y-rub} \end{bmatrix} = -H(e-\delta_0)\frac{(e-\delta_0)k_r}{e}\begin{bmatrix} 1 & -f \\ f & 1 \end{bmatrix}\begin{bmatrix} x_1 \\ y_1 \end{bmatrix} \tag{25}$$

where H(x) indicates the Heaviside function and is defined by Eq. (26).

$$H(x) = \begin{cases} 0 & x<0 \\ 1 & x \geq 0 \end{cases} \tag{26}$$

Nonlinear Oil Film Force in Bearings

A more accurate analysis of the nonlinear oil film force in journal bearings on the lateral vibrations of a hydroturbine is conducted via this force [31], which is expressed via Eq. (27). The variables for this equation are obtained from Eqs. (28) and (29). Additionally, η, G, V, and S used in Eq. (29) are derived from Appendices (54)–(57).

$$\begin{cases} F_{x-oil} = \sigma \overline{f}_{x-ym} \\ F_{y-oil} = \sigma \overline{f}_{y-ym} \end{cases} \tag{27}$$

$$\sigma = \mu_b \omega R_b L_b \left(\frac{R_b}{c_z}\right)^2 \left(\frac{L_b}{2R_b}\right)^2 \tag{28}$$

$$\begin{bmatrix} \overline{f}_{x-ym} \\ \overline{f}_{y-ym} \end{bmatrix} = \frac{\left[(x_2 - 2\dot{y}_2)^2 + (y_2 + 2\dot{x}_2)^2\right]^{\frac{1}{2}}}{1 - x_2^2 - y_2^2} \begin{bmatrix} 3x_2 V(x_2, y_2, \eta) - \sin\eta G(x_2, y_2, \eta) - 2\cos\eta S(x_2, y_2, \eta) \\ 3y_2 V(x_2, y_2, \eta) + \cos\eta G(x_2, y_2, \eta) - 2\sin\eta S(x_2, y_2, \eta) \end{bmatrix} \tag{29}$$

where R_b, L_b, μ_b, ω, and c_z are the radius of the journal bearing, the length of the journal bearing, the viscosity of the oil, the rotational speed of the shaft, and the radial clearance between the shaft and the bearing, respectively.

Nonlinear Force Due to the Seal

Labyrinth seals are widely used in turbomachinery to prevent fluid leakage. Similarly, fluid forces on a turbine's labyrinth seal significantly impact the dynamic behavior of hydroturbine generator units. In this study, the effect of the nonlinear seal force, along with the nonlinear bearing force, is applied to the hydroturbine runner for the first time and is expressed by Eq. (30) [25].

$$\begin{aligned} \begin{bmatrix} F_{x-seal} \\ F_{y-seal} \end{bmatrix} = & \begin{bmatrix} m_f\tau_f^2\omega^2 - K & -\tau_f\omega D \\ \tau_f\omega D & m_f\tau_f^2\omega^2 - K \end{bmatrix}\begin{bmatrix} x_2 \\ y_2 \end{bmatrix} \\ & - \begin{bmatrix} D & 2m_f\tau_f\omega \\ -2m_f\tau_f\omega & D \end{bmatrix}\begin{bmatrix} \dot{x}_2 \\ \dot{y}_2 \end{bmatrix} \\ & - \begin{bmatrix} m_f & 0 \\ 0 & m_f \end{bmatrix}\begin{bmatrix} \ddot{x}_2 \\ \ddot{y}_2 \end{bmatrix} \end{aligned} \tag{30}$$

where K, D, τ_f, ω, and c_s are the equivalent fluid stiffness, equivalent damping, fluid inertia coefficient, rotational speed of the shaft, and radial clearance between the shaft and the seal, respectively, and are expressed by Eq. (31).

$$\begin{cases} K = K_0(1 - e_s^2)^{-n} \\ D = D_0(1 - e_s^2)^{-n} \\ \tau_f = \tau_0(1 - e_s)^b \\ e_s = \sqrt{x_2^2 + y_2^2}/c_s \end{cases} \tag{31}$$

Centrifugal Force Due to Arcuate Whirl

Owing to the centrifugal force, the arcuate whirl of the generator and the hydroturbine runner occurs around the geometric centerline, resulting in rotor deviation from the bearing center [15]. This phenomenon introduces a new force F_G to the rotor, which is expressed by Eq. (32). W, g, ω, and r are the rotational inertia of the rotating part, gravitational acceleration, rotational speed, and radius of arcuate whirl, respectively.

$$F_G = \frac{W}{g}\omega^2 r \tag{32}$$

The total rotational inertia of generator W_1 and the total rotational inertia of hydroturbine runner W_2 can be expressed by Eq. (33).

$$\begin{cases} W_1 = J_1 + 2m_1e_1^2 \\ W_2 = J_2 + 2m_2e_2^2 \end{cases} \tag{33}$$

The arcuate whirl radius of the generator is considered equal to the average arcuate whirl radius of the upper and lower support bearings, and according to Eqs. (4) and (5), r_G is expressed by Eq. (34).

$$r_G = \frac{r_3 + r_4}{2} \tag{34}$$

Similarly, the arcuate whirl radius of the hydroturbine runner is considered equal to the radius of the hydroturbine support bearing, and according to Eq. (6), r_T is expressed by Eq. (35).

$$r_T = r_5 \tag{35}$$

By substituting the arcuate whirl radius and the rotational inertia into Eq. (32), the centrifugal forces of the generator and the hydroturbine, F_{GG} and F_{GT}, are expressed by Eq. (36), respectively.

$$\begin{aligned} F_{GG} &= \frac{\left(J_1 + 2m_1e_1^2\right)(r_3 + r_4)\omega^2}{2g} \\ F_{GT} &= \frac{\left(J_2 + 2m_2e_2^2\right)\omega^2 r_5}{g} \end{aligned} \tag{36}$$

Governing Equations

Under lateral-torsional vibrations, the rotational angles of the generator and the hydroturbine are defined according to Eq. (37), where ϕ_1 and ϕ_2 are the initial rotational angles of the generator rotor and the hydroturbine runner, respectively, and the difference between these two angles is denoted as θ.

$$\begin{cases} \varphi_1 = \int \dot{\varphi}_1 dt + \phi_1 \\ \varphi_2 = \int \dot{\varphi}_2 dt + \phi_2 \\ \theta = \varphi_1 - \varphi_2 = \phi_1 - \phi_2 \end{cases} \tag{37}$$

$$\begin{aligned}
\ddot{x}_1 &= \frac{1}{m_1}\left(F_{GG}\cos\varphi_1 + F_{x-ump} + F_{x-rub} - K_{12}x_1\frac{\sqrt{x_2^2+y_2^2}}{\sqrt{x_1^2+y_1^2}} - c_1\dot{x}_1 + m_1e_1\dot{\varphi}_1^2\cos\varphi_1 - 2K_{11}x_1 - \mu\alpha_x\right) \\
\ddot{y}_1 &= \frac{1}{m_1}\left(F_{GG}\sin\varphi_1 + F_{y-ump} + F_{y-rub} - y_1\frac{\sqrt{x_2^2+y_2^2}}{\sqrt{x_1^2+y_1^2}}K_{12} - c_1\dot{y}_1 + m_1e_1\dot{\varphi}_1^2\sin\varphi_1 - 2y_1K_{11} - \mu\alpha_y\right) \\
\ddot{x}_2 &= \frac{1}{m_2}\left(F_{GT}\cos\varphi_2 + F_{x-seal} + F_{x-oil} - x_2\frac{\sqrt{x_1^2+y_1^2}}{\sqrt{x_2^2+y_2^2}}K_{12} - c_2\dot{x}_2 + m_2e_2\dot{\varphi}_2^2\cos\varphi_2 - 2x_2K_{22}\right) \\
\ddot{y}_2 &= \frac{1}{m_2}\left(F_{GT}\sin\varphi_2 + F_{y-seal} + F_{y-oil} - y_2\frac{\sqrt{x_1^2+y_1^2}}{\sqrt{x_2^2+y_2^2}}K_{12} - c_2\dot{y}_2 + m_2e_2\dot{\varphi}_2^2\sin\varphi_2 - 2y_2K_{22}\right) \\
\ddot{\alpha}_x &= \frac{1}{J_d}\left(-c_3\dot{\alpha}_x - J_p\,\dot{\varphi}_1\dot{\alpha}_y - \mu x_1 - \delta\alpha_x\right) \\
\ddot{\alpha}_y &= \frac{1}{J_d}\left(-c_3\dot{\alpha}_y - J_p\,\dot{\varphi}_1\dot{\alpha}_x - \mu y_1 - \delta\alpha_y\right) \\
\ddot{\theta} &= \frac{m_2e_2\ddot{y}_2\cos\varphi_2 - m_2e_2\ddot{x}_2\sin\varphi_2}{\left(j_2 + 2m_2e_2^2\right)} - \frac{m_1e_1\ddot{y}_1\cos\varphi_1 - m_1e_1\ddot{x}_1\sin\varphi_1}{\left(j_1 + 2m_1e_1^2\right)} - \frac{M_g}{j_1 + 2m_1e_1^2} - \frac{M_t}{j_2 + 2m_2e_2^2} \\
&\quad - k_y\theta\frac{\left(j_2 + 2m_2e_2^2 + j_1 + 2m_1e_1^2\right)}{\left(j_2 + 2m_2e_2^2\right)\left(j_1 + 2m_1e_1^2\right)} - \frac{J_p}{2\left(j_1 + 2m_1e_1^2\right)}\left(\ddot{\alpha}_x\alpha_y - \ddot{\alpha}_y\alpha_x\right) - c_t\dot{\theta}
\end{aligned} \tag{38}$$

Torsional vibrations are caused primarily by torsional damping forces, centrifugal forces of the rotor, torsional elasticity torque of the rotating spindle, external forces acting on the system, and the inertia torque of the hydroturbine. Since both the hydroturbine and generator have the same angular velocity, it can be assumed that $\dot{\varphi}_1 = \dot{\varphi}_1 = \omega$. Additionally, under stable operating conditions of the hydroturbine-generator set, the angular accelerations of both components are zero ($\ddot{\varphi}_1 = \ddot{\varphi}_2 = 0$).

Therefore, the equation governing the lateral-torsional vibrations of the stable state of the hydroturbine-generator set can be obtained by substituting the kinetic energy, potential energy, and derived forces into the coupled differential Eq. (38).

Results and Discussion

The governing Eqs. (38), sre solved numerically to obtain vibration responces of hydroturbine and generator rotors. The parameters values and simulation procedure are described in the "Simulation Procedure" section. Solution of Eqs. (38) give vibration responces which are amplitude versus time. The diagram of displacement amplitude versus time are plotted and analyzed as time signals in "Time-Domain Vibration Response" section. To investigate frequency content of vibration signals, the Fast Fourier Transform (FFT) is utilized. The frequency spectrums obtained from FFT are plotted in "Frequency Spectrum" section and analyzed. To analysis the chaotic behavior in vibration responses, phase plane and Poincare section are obtained and plotted. The phase plane and Poincare section plots are analyzed and discussed in "Phase Plane" section and "Poincare Section" section.

Simulation Procedure

To ensure the accuracy of the result, vibration responces of hydroturbine and generator rotors are obtained based on model of Ref. [24]. They developed a mathematical model of the coupled hydroturbine-generator system with multi-degree of freedom incorporating the effects of gyroscopic forces, linear oil film forces in the bearings, mass imbalance, and the force of unbalance magnetic pull. The study also examines the vibration responses at different rotational speeds (20, 60, 80, and 120 rad/s).

The governing equations are solved numerically by RK4, and the vibration responses of the generator and hydroturbine are obtained. The time step for solving the numerical equations is set at 0.1 s, and the total simulation time is 40 s. The x_1 and y_1 correspond to the lateral vibrations of the generator, while x_2 and y_2 represent the lateral vibrations of the hydroturbine.

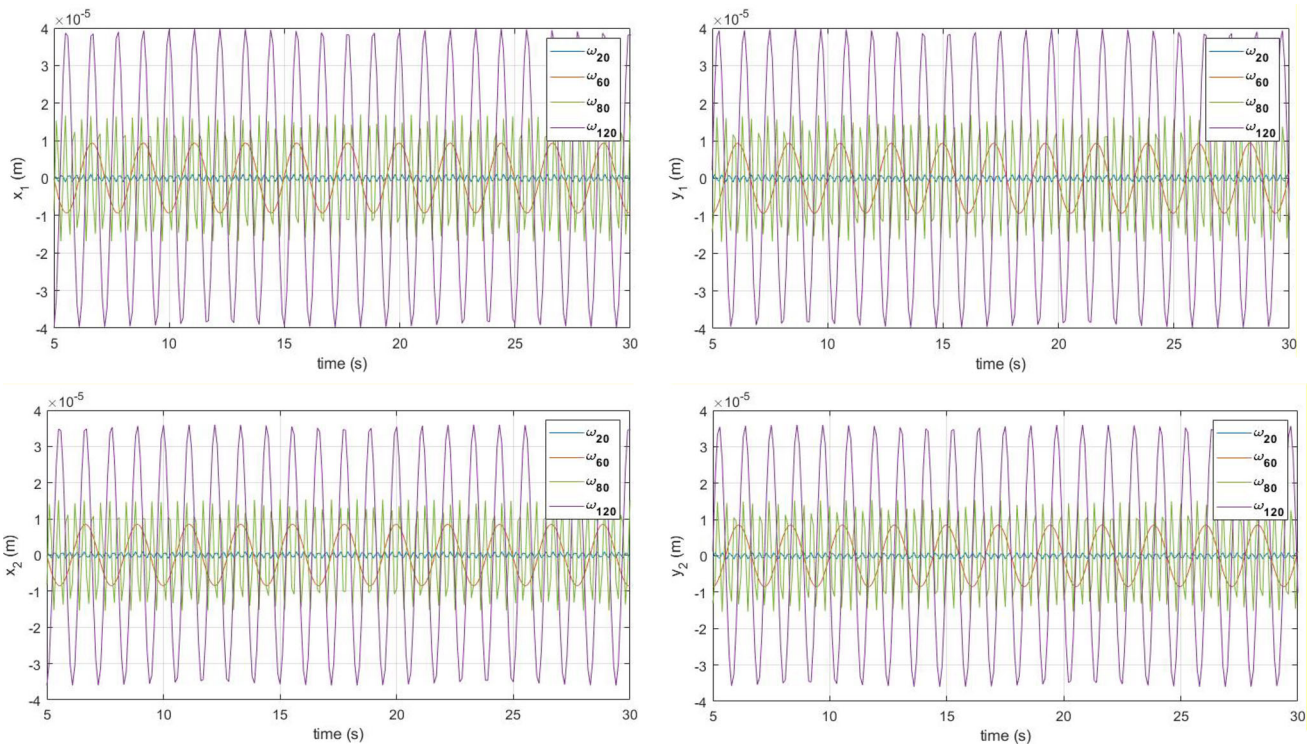

Fig. 4 Vibration response of hydroturbine-generator rotor based on model proposed in Ref. [24]

Table 1 Values of the mechanical parameters

Parameter	Value
Mass of the generator rotor (m_1)	6.28×10^5 (kg)
Mass of the hydroturbine runner (m_2)	3.73×10^5 (kg)
Upper bearing stiffness of the generator rotor (k_1)	2.5×10^9 (N/m)
Lower bearing stiffness of the generator rotor (k_2)	0.9×10^9 (N/m)
Bearing stiffness of the hydroturbine (k_3)	0.8×10^9 (N/m)
Damping coefficient of the generator rotor bearings (c_1)	3×10^4 (N s/m)
Damping coefficient of the hydroturbine runner bearings (c_2)	4×10^4 (N s/m)
Structural damping coefficient of the generator rotor (c_3)	4×10^4 (N s/m)
Mass eccentricity of the generator rotor (e_1)	0.5×10^{-3} (m)
Mass eccentricity of the hydroturbine runner (e_2)	0.5×10^{-3} (m)
Inertia of the generator rotor (J_1)	5.84×10^6 (kg/m^2)
Inertia of the hydroturbine runner (J_2)	2.65×10^6 (kg/m^2)
Inertia of the generator rotor about the axis of rotation (J_p)	5.84×10^6 (kg/m^2)
Inertia of the generator rotor about the axis diameter (J_d)	2.92×10^6 (kg/m^2)
Spring constant of the generator shaft against force F (δ)	6.5×10^8 (N/m)
Spring constant of the generator shaft against moment M (μ)	9×10^7 (N/m)
Center distance of the upper bearing and generator rotor (a)	3.75 (m)
Center distance of the generator rotor and lower bearing (b)	0.5 (m)
Center distance of the lower bearing and turbine support (c)	7.5 (m)
Center distance of the turbine support and hydroturbine runner (d)	3.75 (m)
Radial stiffness of the stator (k_r)	5×10^8 (N/m)
Friction coefficient between rotor and stator (f)	0.01
Viscosity coefficient of bearing oil (μ_b)	2.4×10^{-2} (Pa s)
Radial clearance between shaft and bearing (c_z)	4×10^{-3} (m)
Journal bearing length (L_b)	0.5 (m)
Radius of the journal bearing (R_b)	0.3 (m)
Length of the labyrinth seal (L_s)	0.5 (m)
Radius of the labyrinth seal (R_s)	0.3 (m)
Linear flow velocity in the seal (v)	3 (m/s)
Hydrodynamic viscosity coefficient (v)	1.3×10^{-3} (Pa s)
Labyrinth seal pressure (ΔP)	5×10^5 (Pa)

Table 2 Values of the electrical parameters

Parameter	Value
Length of the generator rotor (L_g)	3 (m)
Radius of the generator rotor (R_g)	6 (m)
Magnetic permeability coefficient (μ_0)	$4\pi \times 10^{-7}$ (H/m)
Excitation current (I_j)	700 (A)
Air gap clearance between rotor and stator (δ_0)	8×10^{-3} (m)
Magnetic resistivity coefficient (k_j)	5.1

Figure 4 presents the vibration response of the generator and hydroturbine based on the model proposed in Ref. [24]. It can be observed that these plots show excellent agreement with reference result in terms of vibration period and amplitude. This confirms that the modeling and solving approach can be effectively used to analyze other effects or to study the system under different operational conditions.

To solve governing equations, the fourth-order Runge–Kutta (RK4) method is implemented in MATLAB software. The RK4 method is a highly accurate numerical technique for solving ordinary differential equations (ODEs), particularly useful in studying the dynamic behavior of vibrating systems. By evaluating the governing equations at multiple intermediate points within each time step, RK4 achieves greater accuracy than simpler methods like the Euler approach.

This method is especially effective for simulating vibrations, capturing key characteristics such as vibrationfrequency, amplitude, and damping effects with

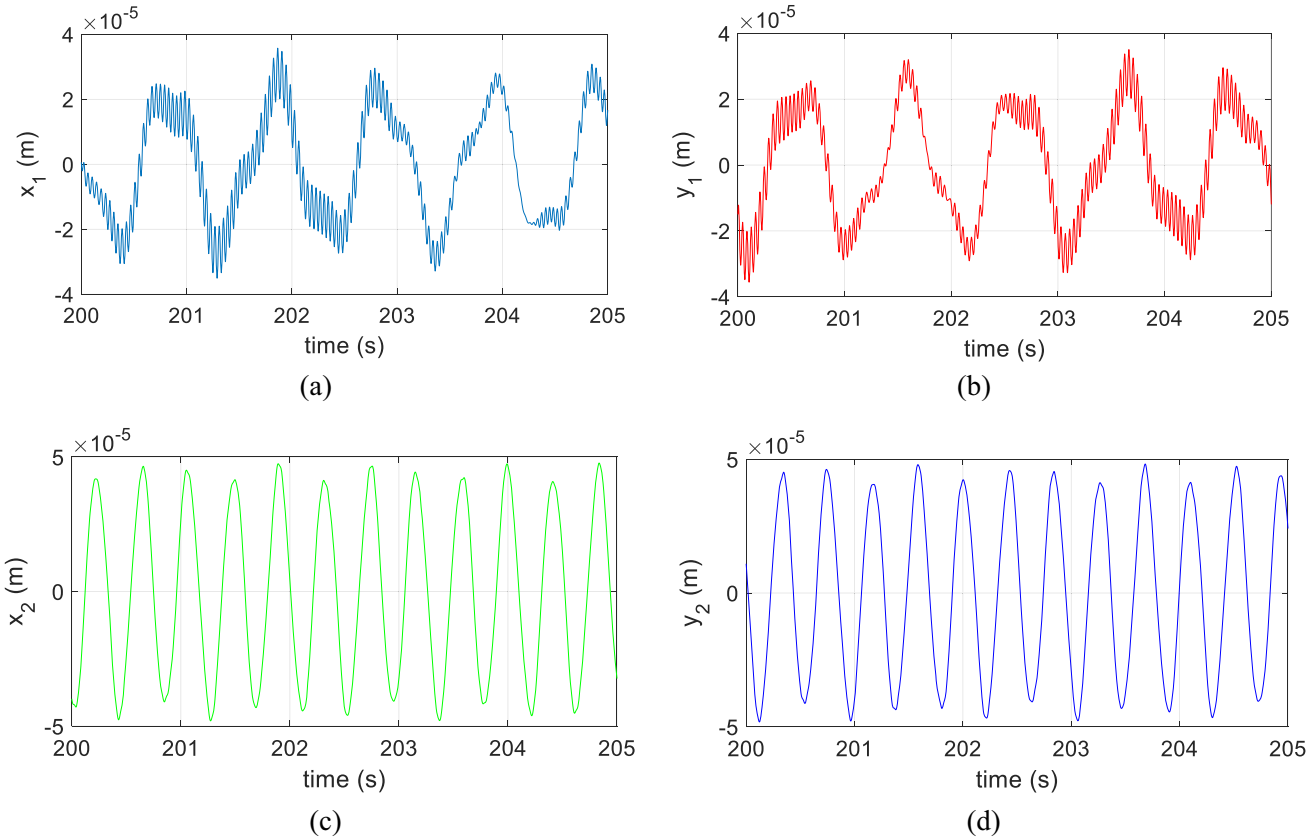

Fig. 5 Lateral vibrations of the generator and hydroturbine at ω = 15 rad/s: **a** x_1, **b** y_1, **c** x_2, **d** y_2

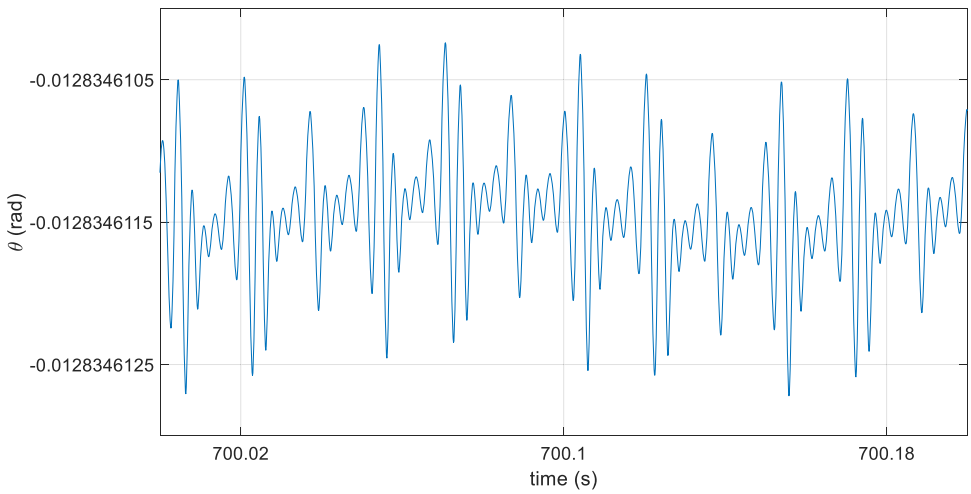

Fig. 6 Torsional vibration of the hydroturbine-generator set at ω = 15 rad/s

precision. It is capable of handling both linear and non-linear systems, as well as complex external forces, making it a versatile tool for dynamic analysis. RK4 strikes a practical balance between computational efficiency and accuracy, making it well-suited for a variety of applications.

A variable time step with a maximum value of 0.001 has been used, which, considering the rotational speed of the hydroturbine, provides a very good resolution, which is also needed to draw phase diagrams. With this choice, convergence of the response was also achieved.

To solve the governing differential equations of the system, numerical values of the mechanical and electrical parameters are required, which are specified in Tables 1 and 2. After the vibrational responses of the system are obtained, time-domain, frequency-domain, phase plane, and Poincare diagrams are utilized for analysis.

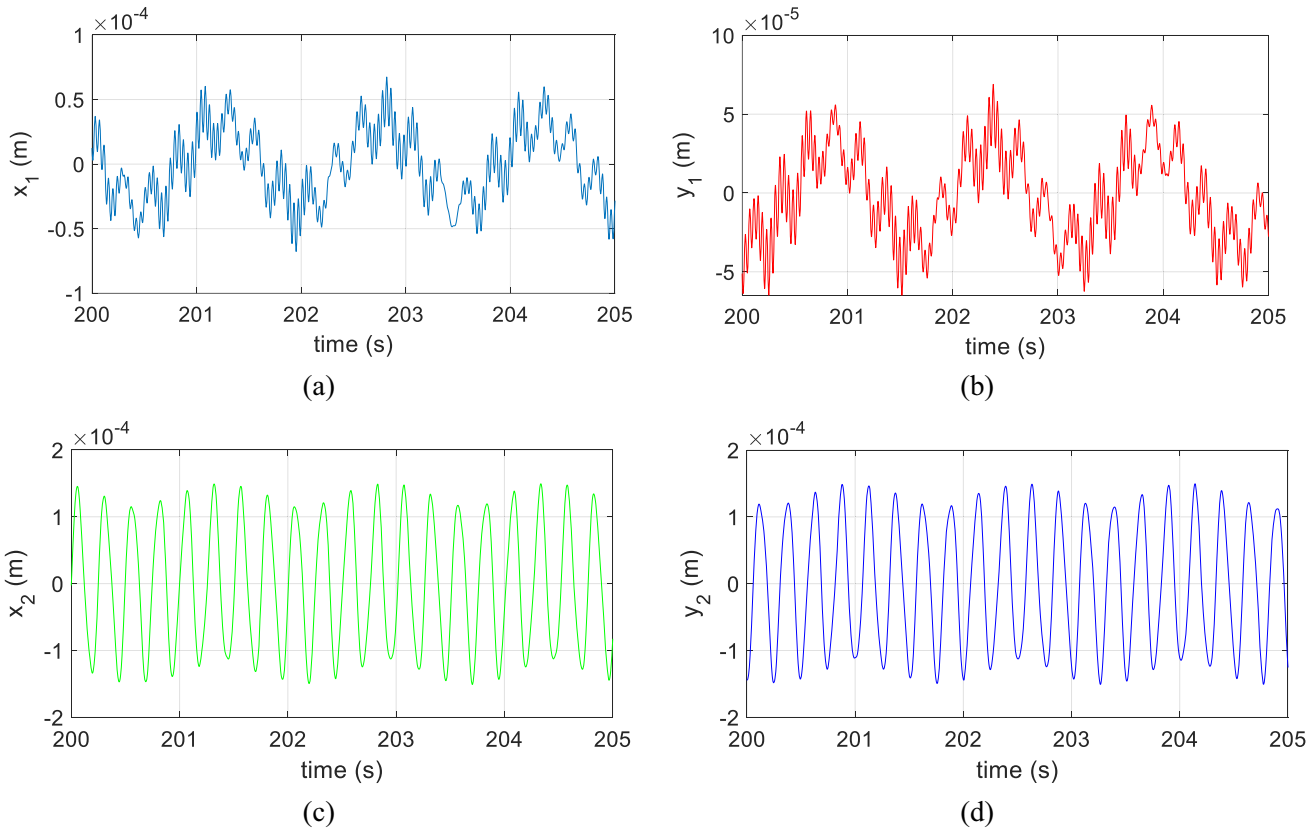

Fig. 7 Lateral vibrations of the generator and hydroturbine at ω = 25 rad/s: **a** x_1, **b** y_1, **c** x_2, **d** y_2

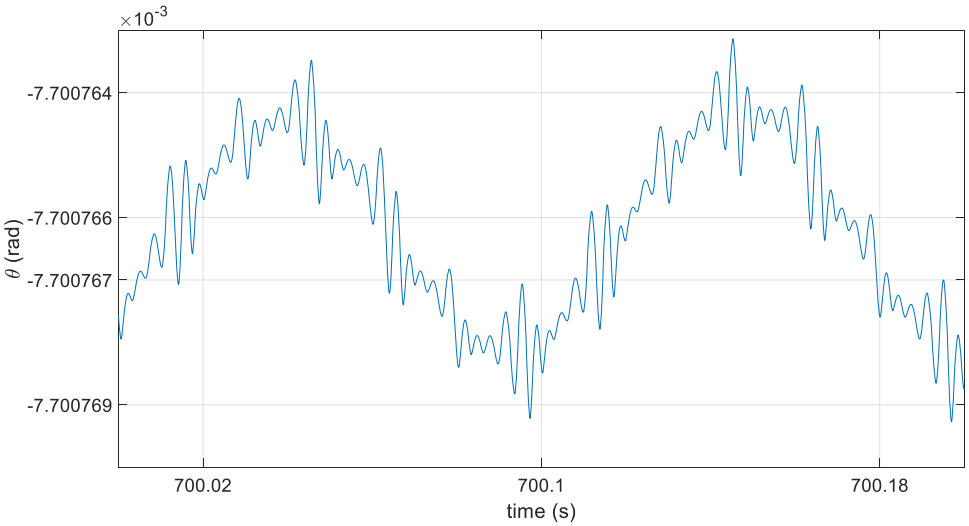

Fig. 8 Torsional vibration of the hydroturbine-generator set at ω = 25 rad/s

Time-Domain Vibration Response

The time-domain plots for lateral-torsional vibrations of the hydroturbine and generator coupling in the x and y directions at rotational speeds of 15, 25, 35, and 45 rad/s are shown in Figs. 5, 6, 7, 8, 9, 10, 11 and 12. According to these plots, as the rotational speed increases, the amplitudes of the vibrations of the generator and hydroturbine increase at different rates. Conversely, with increasing rotational speed, the modulation of the torsional vibration amplitude θ decreases.

The lateral-torsional vibration plots of the hydroturbine-generator set at a rotational speed of 15 rad/s are shown in Figs. 5 and 6, respectively. Figure 5a, b depict the vibrations of the generator, which show noticeable amplitude modulation. Additionally, various frequencies are visible

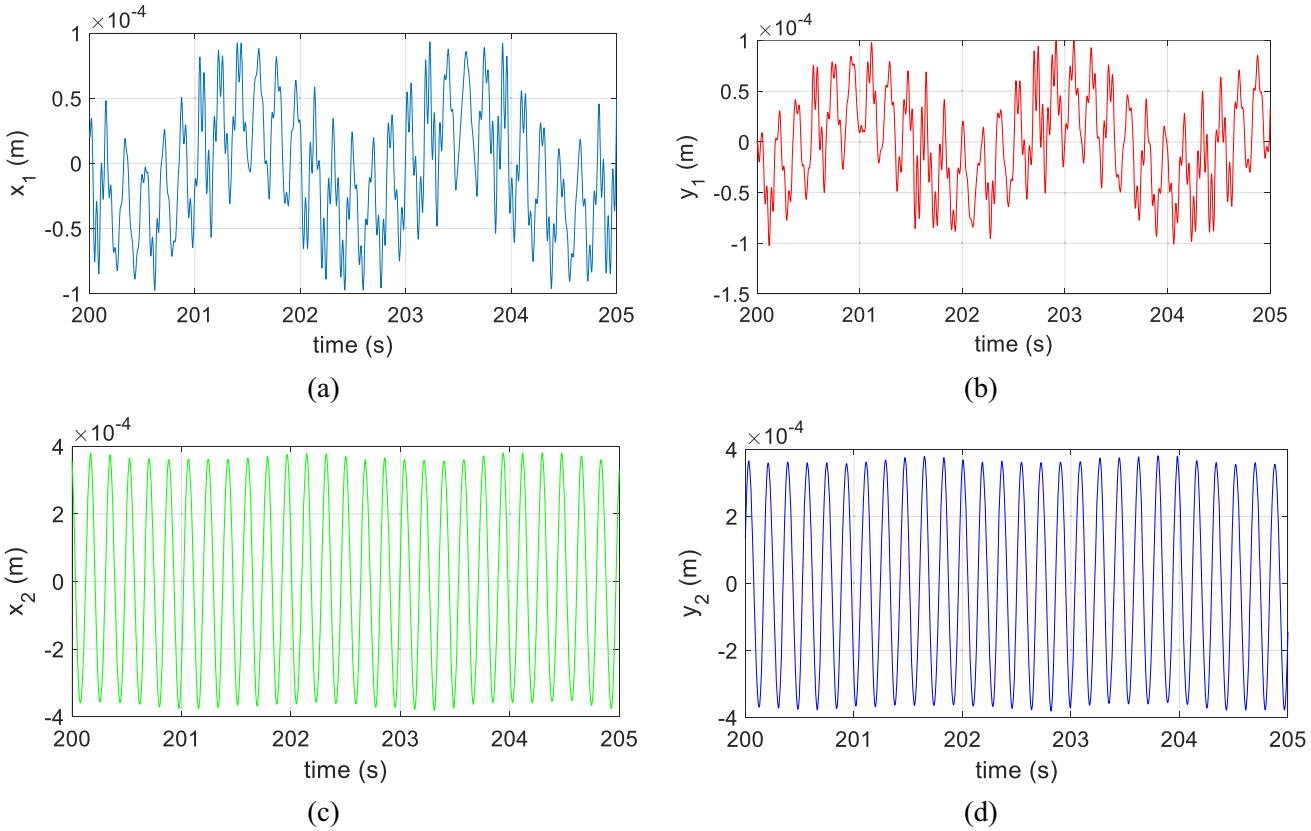

Fig. 9 Lateral vibrations of the generator and hydroturbine at ω = 35 rad/s: **a** x_1, **b** y_1, **c** x_2, **d** y_2

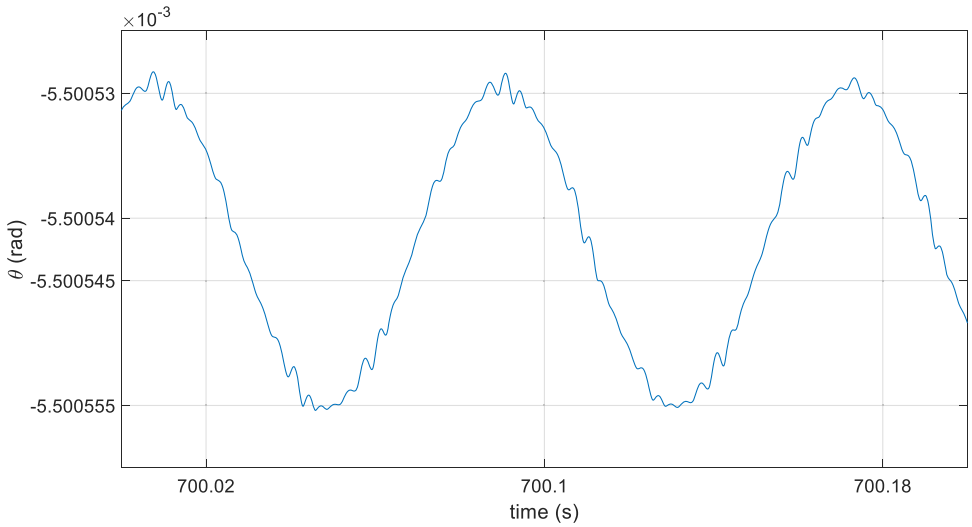

Fig. 10 Torsional vibration of the hydroturbine-generator set at ω = 35 rad/s

where high-frequency vibrations are superimposed on low-frequency vibrations, with a significant increase observed in the amplitude of high-frequency vibrations according to the specified sections of the plot.

For a more detailed examination of the different frequencies in this system, its frequency spectrum will be analyzed in the next section. The irregular appearance of these plots is also attributed to low-frequency phenomena, potentially indicating disturbance in the system, which can be further clarified through frequency spectrum analysis and phase plane plots. Figure 5c, d show that the vibrations of the hydroturbine exhibit harmonic and periodic behavior. The presence of multiple discrete frequencies and coherence in these plots is observable. These observations are further confirmed and complemented by examining the frequency spectrum and phase plane diagrams.

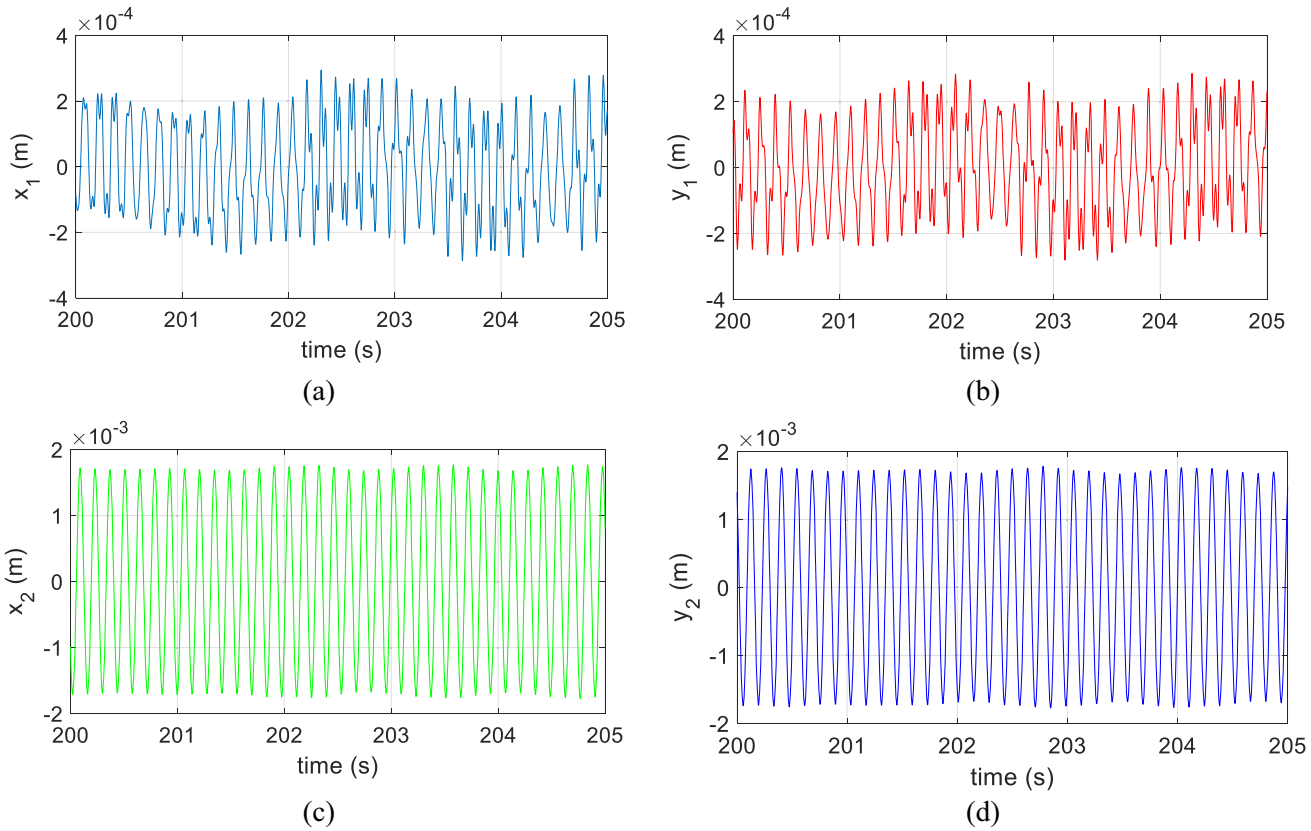

Fig. 11 Lateral vibrations of the generator and hydroturbine at ω = 45 rad/s: **a** x_1, **b** y_1, **c** x_2, **d** y_2

Fig. 12 Torsional vibration of the hydroturbine-generator set at ω = 45 rad/s

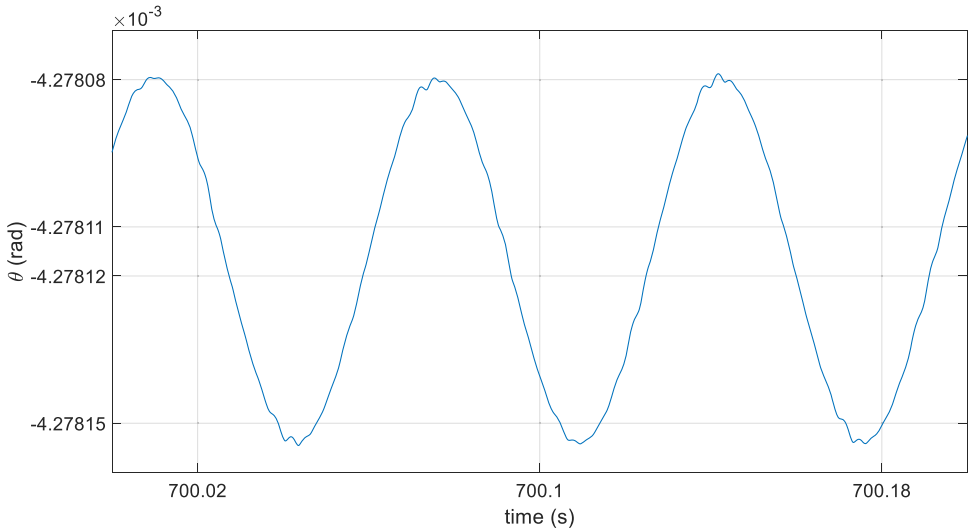

Figure 6 shows the torsional vibrations of the hydroturbine-generator set at a rotational speed of 15 rad/s, represented by θ. This plot reveals the presence of multiple observable frequencies, as well as amplitude modulation within this signal. The frequencies associated with these vibrations can be identified via frequency spectrum plots in the subsequent section.

The response of the generator and hydroturbine vibrations at a rotational speed of 25 rad/s is depicted in Fig. 7. Figure 7a, b illustrate the vibrations of the generator, showing amplitude modulation and the combination of multiple frequencies. Additionally, high-frequency vibrations are superimposed on low-frequency vibrations in these plots.

According to Fig. 7, compared with Fig. 5, the low-frequency vibrationappears more regular, indicating reduced disturbance in the system. Additionally, the amplitude of high-frequency vibrations has noticeably increased, as evident from the plotted data. These effects illustrate the influence of torsional vibrations on lateral vibrations.

For a more detailed analysis, frequency spectrum analyses will be conducted in subsequent sections. The vibration response of the hydroturbine is plotted in Fig. 7c, d, which illustrates the harmonic and periodic behavior as well as the combination of frequencies.

Figure 8 depicts the torsional vibrations of the hydroturbine-generator set at a rotational speed of 25 rad/s. These plots show multiple observable frequencies, with high-frequency vibrations superimposed on low-frequency vibrations. Using the frequency spectrum plots in the subsequent section, the frequencies associated with these vibrations can be identified. The amplitude of vibrations has decreased compared with a rotational speed of 15 rad/s, indicating a reduction in vibration magnitude. Additionally, the behavior has become more periodic and regular.

The time-domain plots of vibrations for the generator and hydroturbine at a rotational speed of 35 rad/s are depicted in Fig. 9. Figure 9a, b present the vibration responses of the generator. In these figures, the generator vibrations include both low-frequency and high-frequency vibrations. In the low-frequency region, a noticeable regularity is observed, whereas irregularities are noticeable in the high-frequency region.

On the basis of the time-domain plots at different rotational speeds, increasing the rotational speed leads to a reduction in the amplitude of high-frequency vibrations. Furthermore, the presence of impacts in these plots indicates that they could be due to a reduced arcuate whirl effect and gyroscopic phenomenon dominating over other effects. The vibrations of the hydroturbine are depicted in Fig. 9c, d, indicating harmonic and periodic behavior. A more detailed examination of frequencies and disturbances will be conducted through frequency spectrum analysis and phase plane diagrams.

Figure 10 shows the vibrations of the angle θ at a rotational speed of 35 rad/s. In this figure, fewer frequencies are observable than in the charts for rotational speeds of 15 and 25 rad/s. High-frequency vibrations are superimposed on low-frequency vibrations, which can be identified via frequency spectrum charts. The amplitude of the vibrations has also decreased compared with the rotational speed of 25 rad/s.

The time-domain charts of the vibrations of the generator and hydroturbine at a rotational speed of 45 rad/s are shown in Fig. 11. Figure 11a, b pertain to the generator, where irregularities in the generator vibrations are still noticeable. The impact of low-frequency vibrations has diminished and impacts are still present. Despite the presence of various vibrations in the generator vibrations, they cannot be considered periodic, which is indicative of chaotic behavior. Figure 11c, d pertain to the hydroturbine. The hydroturbine vibrations remain regular and periodic with a limited number of frequencies.

Figure 12 depicts the vibrations of the angle θ at a rotational speed of 45 rad/s. In this plot, a regular and periodic oscillatory response with a small number of observable frequencies is evident. The amplitude of high-frequency vibrations has decreased, and the corresponding frequencies can be identified via the frequency spectrum figure. Additionally, the amplitude of the vibrations has decreased compared with a rotational speed of 35 rad/s.

Frequency Spectrum

Frequency spectrum charts of the lateral-torsional coupled vibrations of the hydroturbine and generator in the x and y directions at rotational speeds of 15, 25, 35, and 45 rad/s are depicted in Figs. 13, 14, 15 and 16. The frequency corresponding to the rotational speed of the shaft is observable in all charts and, in some cases, it is the highest peak.

In Fig. 13, the lateral vibrations of the generator and hydroturbine at a rotational speed of 15 rad/s are depicted. In Fig. 13a, b, the frequency spectrum of the generator's lateral vibrations is shown. In these figures, two high peaks f_g and f_r are observable, which correspond to frequencies of 0.979Hz and 2.389Hz, respectively. The first high peak is related to the gyroscopic phenomenon, and the second high peak corresponds to the rotational speed of the shaft, which is 15rad/s, derived from Eq. (39).

$$f_r = \frac{\omega}{2\pi} = \frac{15}{2\pi} = 2.3873 \text{ (Hz)} \tag{39}$$

The third and fourth high peaks in this range, which correspond to frequencies of 4.34 Hz and 5.75 Hz respectively, are formed from the combination of the two frequencies f_g and f_r and are derived from Eqs. (40) and (41).

$$f_r + 2f_g = 4.34 \text{ (Hz)} \tag{40}$$

$$2f_r + f_g = 5.75 \text{ (Hz)} \tag{41}$$

The subsequent high peaks are high-frequency vibrations that are generated at equal intervals of 3.36 Hz from these two peaks, which can be calculated according to Eq. (42).

$$f_r + f_g = 3.36 \text{ (Hz)} \tag{42}$$

Additionally, harmonics related to rotational speed are also present in the frequency spectrum of the hydroturbine

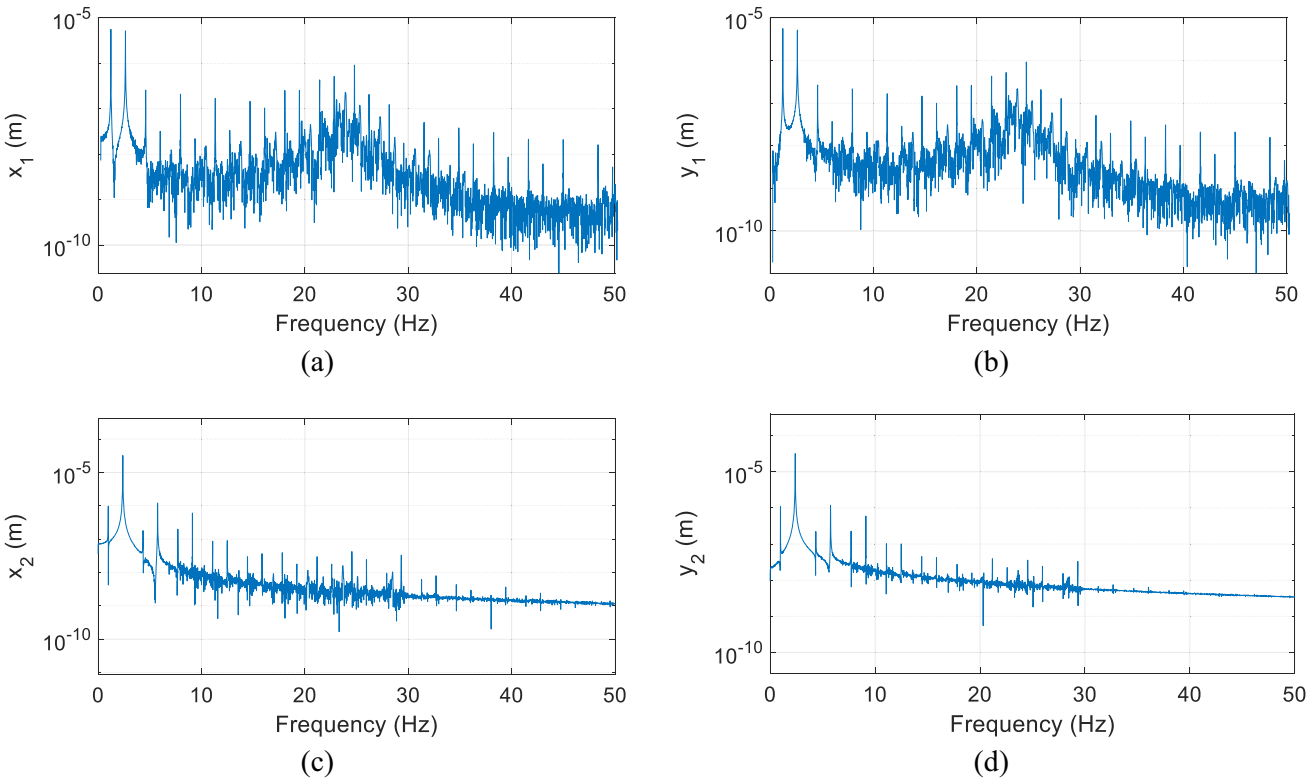

Fig. 13 Frequency spectrum of the generator and hydroturbine lateral vibrations at ω = 15 rad/s: **a** x_1, **b** y_1, **c** x_2, **d** y_2

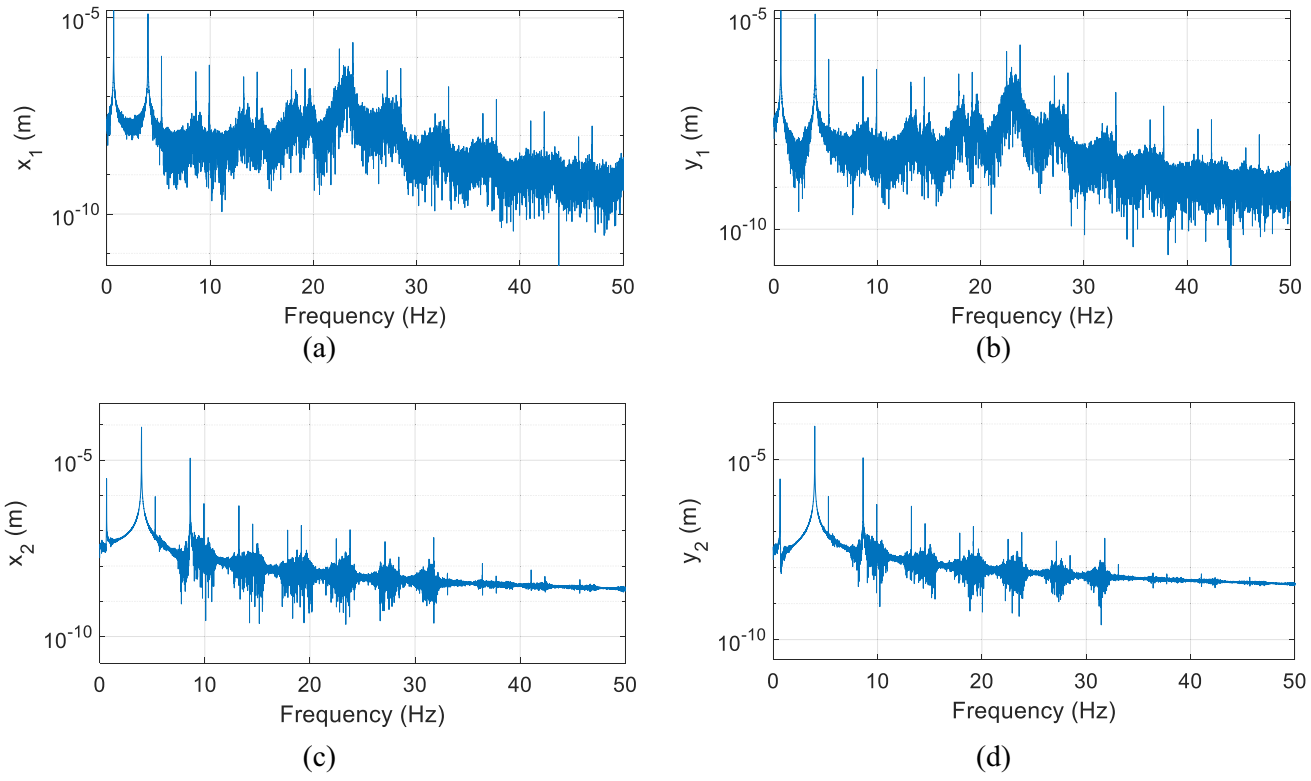

Fig. 14 Frequency spectrum of the generator and hydroturbine lateral vibrations at ω = 25 rad/s: **a** x_1, **b** y_1, **c** x_2, **d** y_2

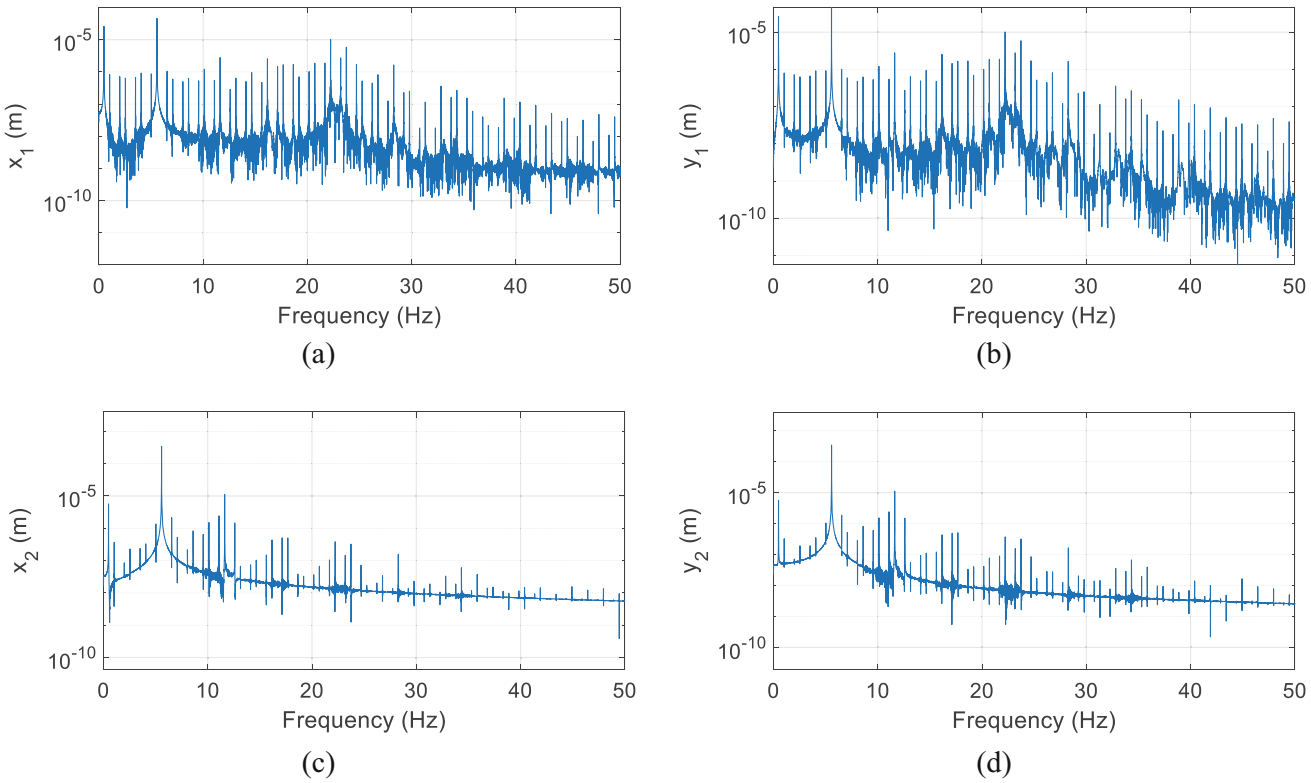

Fig. 15 Frequency spectrum of the generator and hydroturbine lateral vibrations at ω = 35 rad/s: **a** x_1, **b** y_1, **c** x_2, **d** y_2

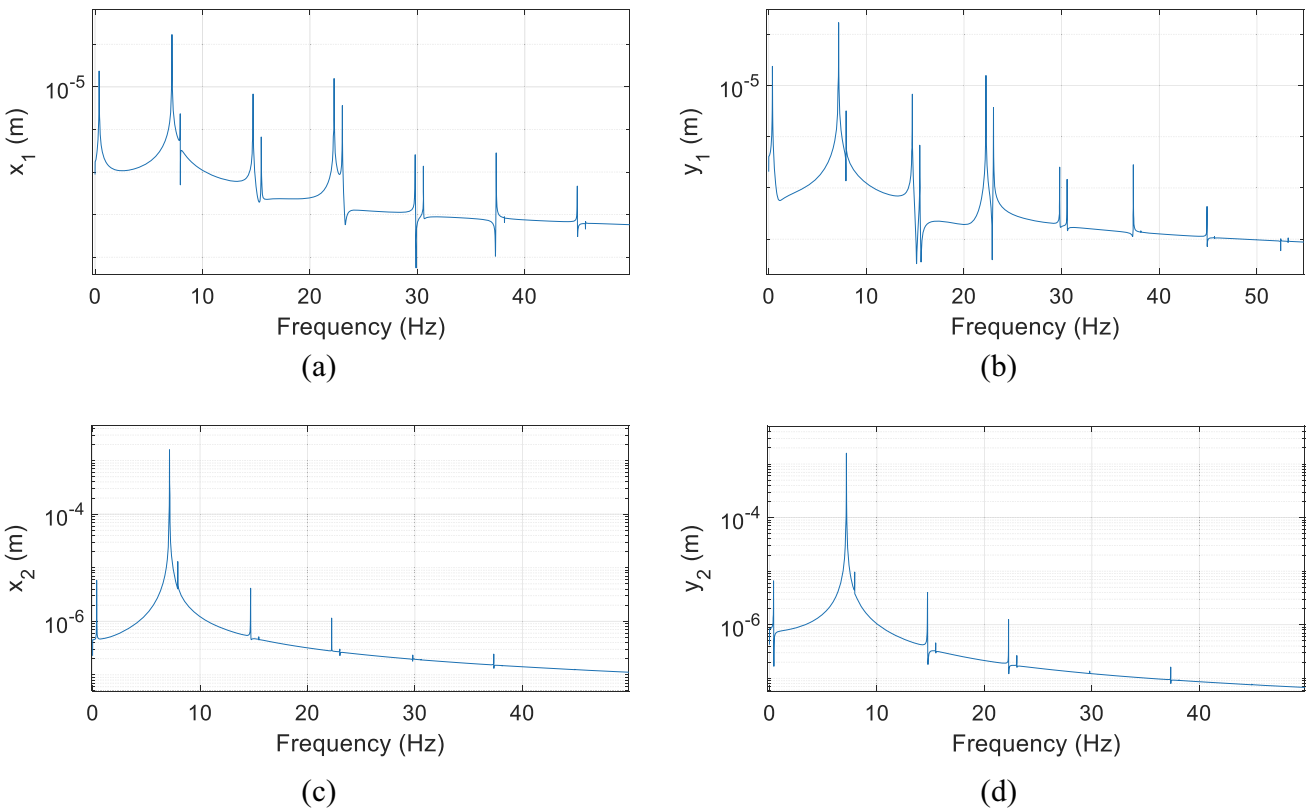

Fig. 16 Frequency spectrum of the generator and hydroturbine lateral vibrations at ω = 45 rad/s: **a** x_1, **b** y_1, **c** x_2, **d** y_2

and generator, but their amplitudes are very small compared with the dominant peaks, indicating the nonlinearity of the system.

The frequency spectrum of the hydroturbine lateral vibrations is shown in Fig. 13c, d. In addition to the frequencies associated with the rotational speed and its harmonics, the spectrum also reveals the frequency f_g with lower intensity. Additionally, in the range of 5Hz to 30Hz, many frequencies, which include combinations of frequencies f_g and f_r, can be observed. These vibrations are generated with very low intensity and have little effect on the hydroturbine vibrations, indicating more periodic motion, which can also be inferred from the time-domain diagrams.

In Fig. 14, the frequency spectra of the generator and hydroturbine lateral vibrations at a rotational speed of 25 rad/s are plotted. In Fig. 14a, b, the frequency spectra of the generator lateral vibrations can be observed. In these figures, there are two tall peaks, f_g and f_r, which correspond to frequencies of 0.655Hz and 3.98Hz, respectively. f_g is the frequency related to the gyroscopic phenomenon, and f_r is the frequency related to the rotational speed of the shaft, which is 25 rad/s and can be calculated as in the previous case. Additionally, the third and fourth tall peaks, which correspond to frequencies of 5.29Hz and 8.61Hz, respectively, are formed by the combination of two frequencies f_g and f_r, according to Eqs. (40) and (41).

The next high peaks in this range, spaced at 4.63Hz intervals from these two peaks, are also created by the sum of the two frequencies f_g and f_r, as in the previous case. The amplitudes of these peaks are smaller than the other peaks. Harmonics of the rotational axis also exist in the frequency spectrum of the hydroturbine and generator. Additionally, many peaks with small amplitudes in the range of 5Hz to 50Hz are observed, indicating disturbances in the generator.

In Fig. 14c, d, the frequency spectra of the hydroturbine lateral vibrations at a rotational speed of 25 rad/s are plotted. In the range of 5Hz to 40Hz, many frequencies with very small amplitudes are observed. Additionally, besides the frequency related to the rotational axis and its harmonics, frequencies such as f_g and combination frequencies also exist with smaller amplitudes, which have little effect on hydroturbine vibrations. This indicates predominantly periodic motion, which is consistent with the observations in the time-domain plots.

The frequency spectra of the generator and hydroturbine lateral vibrations at a rotational speed of 35rad/s are plotted in Fig. 15. In Fig. 15a, b, the frequency spectrum of the generator vibrations is observed, showing the dominant peaks f_g and f_r. These correspond to frequencies related to the gyroscopic phenomenon and the rotational speed of the shaft, which are 0.484 Hz and 5.569 Hz, respectively.

According to the frequency spectrum of the generator, four high peaks corresponding to frequencies of 6.54Hz, 11.63Hz, 12.59Hz, and 17.68Hz are created by the combination of two frequencies f_g and f_r, which can be calculated via Eqs. (43) to (46). Additionally, the remaining high peaks in this range are spaced at equal frequency intervals of 4.6Hz from these four peaks, which can be calculated according to Eq. (47).

$$f_r + 2f_g = 6.54\ (\text{Hz}) \tag{43}$$

$$2f_r + f_g = 11.63\ (\text{Hz}) \tag{44}$$

$$2f_r + 3f_g = 12.59\ (\text{Hz}) \tag{45}$$

$$3f_r + 2f_g = 17.68\ (\text{Hz}) \tag{46}$$

$$f_r - 2f_g = 4.6\ (\text{Hz}) \tag{47}$$

Harmonics of the rotational axis and gyroscopic frequencies also exist in the frequency spectrum of the hydroturbine and generator as integer multiples, indicating the nonlinearity of the system. According to Fig. 15, compared with Fig. 14, a significant number of peaks with smaller amplitudes in the range of 5Hz to 50Hz are observed. These peaks suggest the presence of chaotic behavior, albeit with lower intensity in the system. This behavior is also observable in the time-domain plots.

In Fig. 15c, d, the frequency spectra of the hydroturbine lateral vibrations at a rotational speed of 35 rad/s are plotted. These plots show that in the range of 5Hz to 40Hz, in addition to the frequencies related to the rotational axis, gyroscopic effects, and their harmonics, there are also combination frequencies with smaller amplitudes. Furthermore, several frequencies with very low amplitudes compared with the dominant peaks are observed in various ranges of the frequency spectrum. These frequencies have little effect on hydroturbine vibrations, indicating predominantly periodic motion, which is also discernible in the time-domain plots.

In Fig. 16, the frequency spectra of the generator and hydroturbine lateral vibrations at a rotational speed of 45 rad/s are plotted. Figure 16a, b depict the frequency spectrum of the generator lateral vibrations, showing two

Table 3 The values of f_r and f_g at different rotational speeds

ω_r(rad/s)	f_r(Hz)	f_g(Hz)	$f_r + f_g$(Hz)
15	2.3873	0.979	3.36
25	3.98	0.655	4.63
35	5.569	0.484	6.1
45	7.16	0.38	7.55

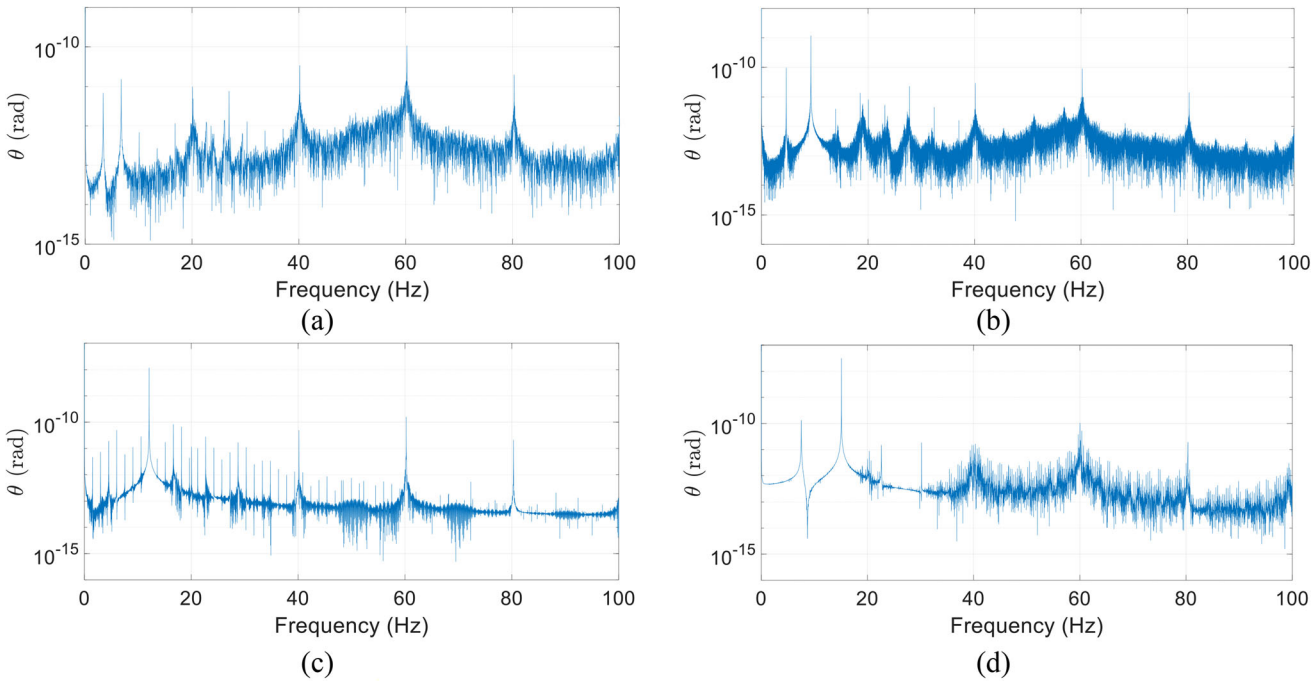

Fig. 17 Frequency spectrum of the torsional vibrations: **a** ω = 15, **b** ω = 25, **c** ω = 35, **d** ω = 45 rad/s

prominent peaks f_g and f_r at frequencies of 0.38Hz and 7.16Hz, respectively, which are calculable as before. Additionally, the third and fourth high peaks in this range, corresponding to frequencies of 7.92Hz and 14.71Hz, respectively, are also visible and are formed by the combination of the two frequencies f_g and f_r according to Eqs. (40) and (41). Similarly, the next high peaks in this range are spaced by 7.55Hz intervals from these two peaks and are created by the combination of f_g and f_r frequencies via Eq. (42).

Furthermore, in the range of 5Hz to 50Hz, according to the frequency diagrams corresponding to rotational speeds of 25 and 35 rad/s, multiple frequencies were present, but they were not observed at a rotational speed of 45 rad/s. However, there may still be disturbances in the system, which can be identified by examining the phase plane and Poincare section diagrams.

In Fig. 16c, d, the frequency spectrum of the hydroturbine lateral vibrations is depicted, where the dominant peak corresponds to the rotational frequency of the shaft. Additionally, the frequency f_g is also observable with very low intensity, confirming the presence of a periodic motion in this plot.

Generally, the frequency values of the peaks shown in Figs. 13, 14, 15 and 16 follow Eqs. (48) and (49). Additionally, the values of f_g, f_r, and the reciprocal of f_g for different rotational speeds are provided in Table 3. Notably, with an increase in rotational speed from 15 to 45 rad/s, the reciprocal of f_g consistently increases by approximately 0.53 units.

$$n(f_r + f_g) + f_r \quad n = 0, 1, 2, \ldots \tag{48}$$

$$n(f_r + f_g) + f_g \quad n = 0, 1, 2, \ldots \tag{49}$$

Figure 17a, b depict the frequency spectra of torsional vibrations of the hydroturbine-generator set, which are essentially torsional vibrations denoted by θ, at rotational speeds of 15 and 25 rad/s, respectively. In these plots, several additional prominent peaks are observable. The primary peaks in each plot, according to Eq. (42), correspond to frequencies of 3.36 Hz and 4.63 Hz, respectively. The other peaks are harmonics of these primary peaks, generated as multiples of their frequencies.

Figure 17c, d display the frequency spectra of torsional vibrations denoted by θ at rotational speeds of 35 and 45 rad/s, respectively. These plots show several high-frequency peaks, with the dominant peak corresponding to frequencies of 12.11 Hz and 15.09 Hz. These values correspond to the sum of two frequencies, f_g and f_r, at rotational speeds of 35 and 45 rad/s, respectively. Additionally, in these figures, owing to the nonlinear nature of the system, harmonics are also observed as integer multiples of these primary frequencies. This phenomenon also supports the periodic motion observed in time-domain plots.

In Fig. 17c, a lower-intensity frequency of 1.51 Hz is present in the spectrum, which accounts for one of the primary vibration frequencies. Additionally, in Fig. 17d, the frequency of 7.55 Hz and its harmonics are also

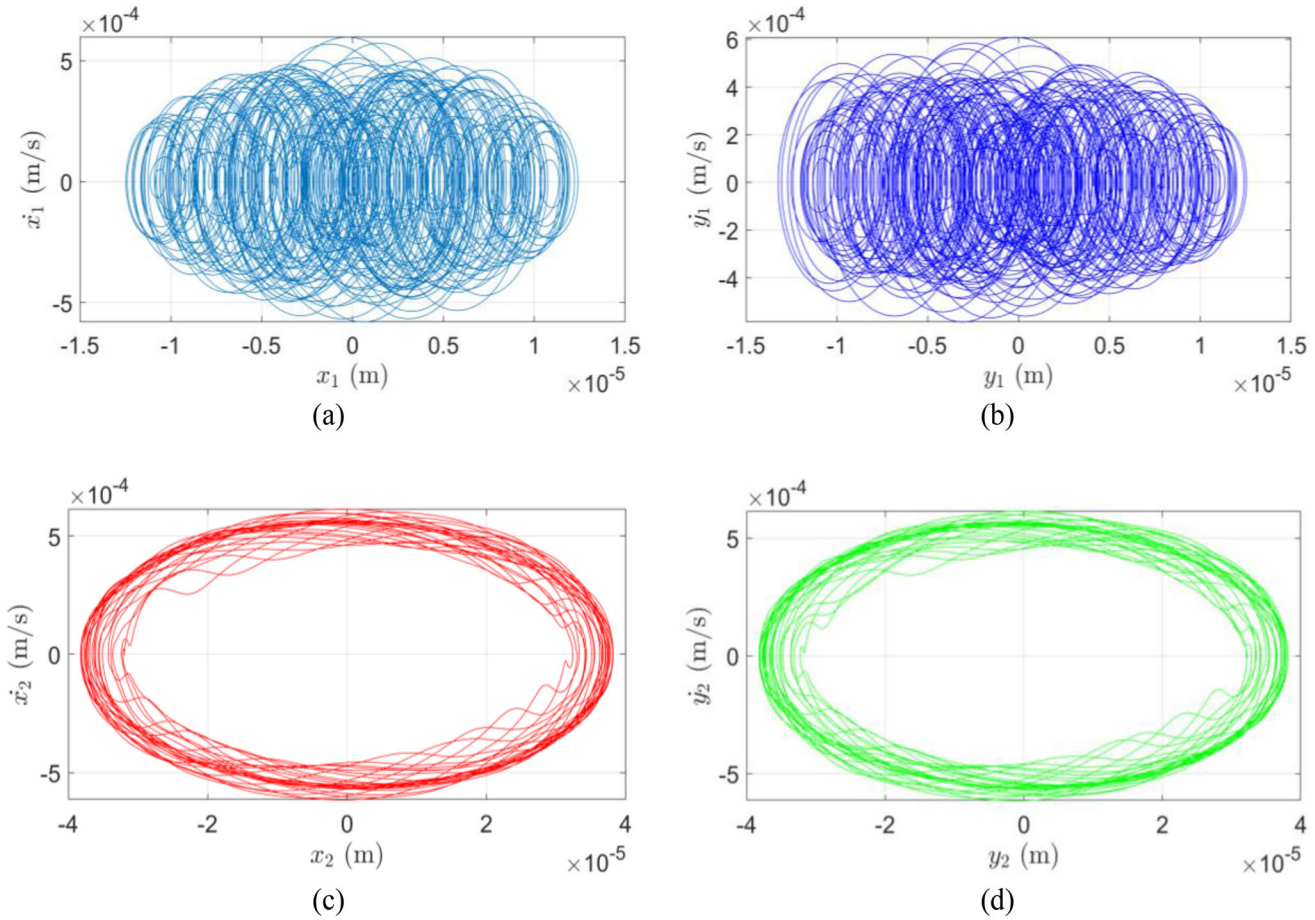

Fig. 18 Phase plane for the generator and hydrotourbine lateral vibrations at ω = 15 rad/s: **a** $\dot{x}_1$–x_1, **b** $\dot{y}_1$–y_1, **c** $\dot{x}_2$–x_2, **d** $\dot{y}_2$–y_2

observable. Generally, the frequency values of the peaks in Fig. 17 adhere to Eq. (50).

$$n(f_r + f_g), n = 0, 1, 2 \tag{50}$$

Phase Plane

To study and analyze the dynamic behavior of nonlinear systems, in addition to time-domain and frequency-domain plots, other tools are also used, with the most famous and widely used being phase plane or phase space diagrams. In phase plane diagrams, various dynamic behaviors, such as harmonic, superharmonic, and subharmonic vibrations, as well as phenomena such as quasiperiodic and chaotic behavior, can be easily observed and analyzed.

As mentioned, the vibration equations used in this paper are second-order equations. Therefore, these equations have two states of displacement and velocity for the vibration variables. According to Figs. 18, 19, 20 and 21, velocity versus displacement is plotted for each vibration variable of the system components, which are referred to as phase planes. These diagrams are two-dimensional phase planes because they depict two states in the equations. Hence, in this work, we do not have a phase space; instead, we have phase planes due to the presence of these two states in the equations.

The phase plane diagrams for the vibrations of this system all exhibit strange attractors. One characteristic of strange attractors is that trajectories diverge from each other but do not tend toward infinity or instability. Instead, all trajectories move within a distinct region that acts as the attractor, pulling all trajectories toward itself. Unlike other types of attractors, such as points, lines, limit cycles, or tori, the shape of a strange attractor is irregular, which is why it is called “strange”.

The existence of a distinct shape for the attractor confirms that the data are not random and follow a specific dynamic pattern. Furthermore, the strange shape of the attractor confirms the nonlinear behavior of the system and the presence of chaos within it. The presence of chaos and the different chaotic behaviors observed in the planetary gearbox components, as evidenced by the phase plane diagrams, are significant findings.

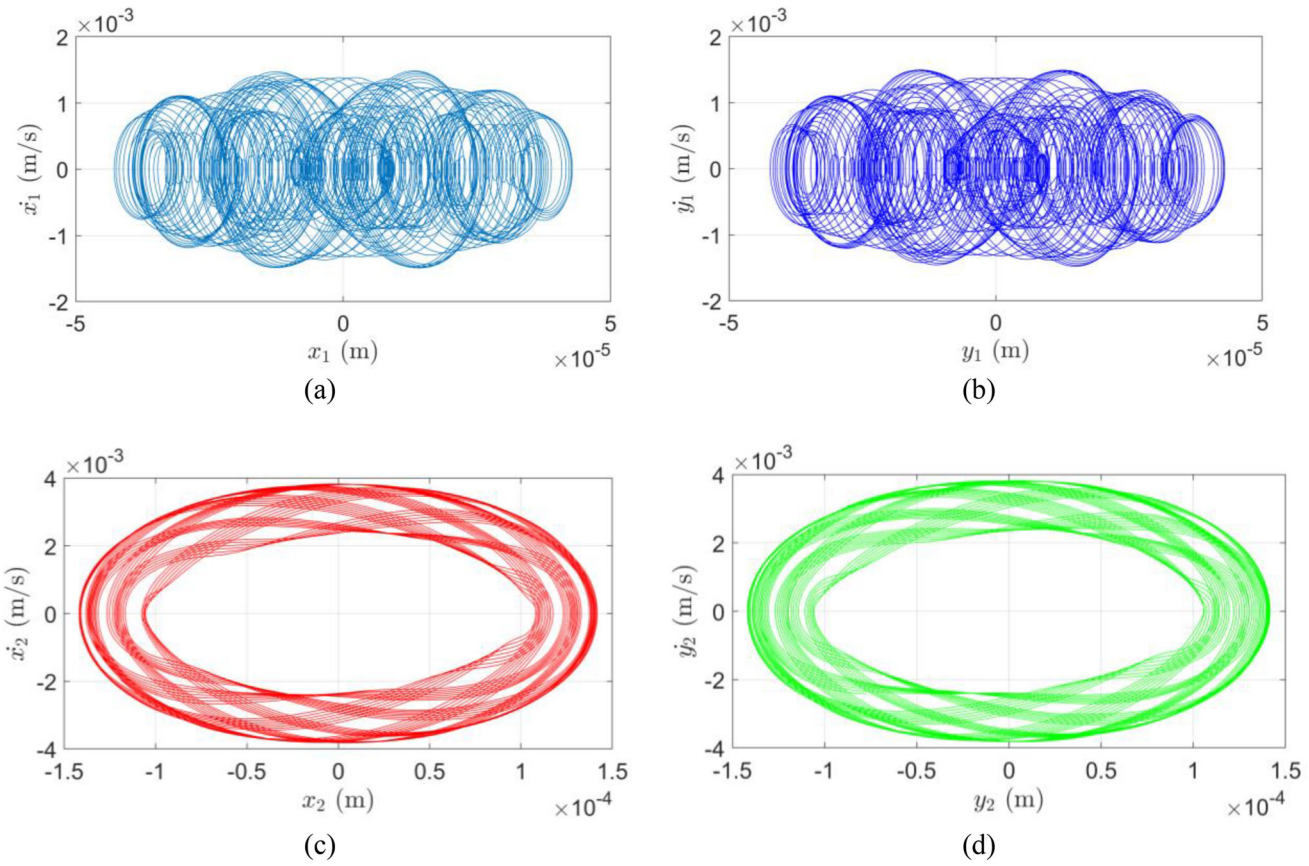

Fig. 19 Phase plane for the generator and hydrotourbine lateral vibrations at ω = 25 rad/s: **a** $\dot{x}_1$–x_1, **b** $\dot{y}_1$–y_1, **c** $\dot{x}_2$–x_2, **d** $\dot{y}_2$–y_2

Phase plane diagrams for the lateral–torsional vibrations of the hydroturbine–generator coupling in both the X and Y directions at rotational speeds of 15, 25, 35, and 45 rad/s are depicted in Figs. 18, 19, 20 and 21. By observing the phase plane diagrams for the generator, quasiperiodic and chaotic dynamic behaviors are apparent. However, in the phase plane diagrams for the hydroturbine, harmonic, superharmonic, and subharmonic dynamic behaviors are observed.

In Fig. 18, phase plane diagrams for the lateral vibrations of the generator and hydroturbine at a rotational speed of 15 rad/s are shown. Figure 18a, b display the phase plane for the generator lateral vibrations, where trajectories around several strange attractors are rotating. Despite their irregular appearance, these trajectories do not move toward instability. Owing to the nonlinear nature of the system equations and this type of dynamic behavior in the phase plane, which are characteristics of chaotic behavior, it indicates the presence of chaos in the system.

Signs and indicators of this dynamic behavior were also evident in the time-domain and frequency-domain plots of the generator vibrations. Figure 18c, d show the phase plane diagrams for the hydroturbine lateral vibrations, where all trajectories revolve around a center. This type of dynamic behavior is quasiperiodic and is also observable in the time-domain and frequency-domain plots.

Figure 19 shows phase plane diagrams of the lateral vibrations of the generator and hydroturbine at a rotational speed of 25 rad/s. Figure 19a, b depict the complex dynamic behavior associated with the generator lateral vibrations. Despite their irregular appearance, these trajectories do not exhibit random or unstable behavior, which is characteristics of chaotic behavior. The paths move similarly to each other but do not repeat like harmonic or periodic behaviors, which is another hallmark of chaos. On the other hand, the phase plane diagram for the hydroturbine lateral vibrations in Fig. 19c, d shows more intricate behavior than the phase plane at a rotational speed of 15 rad/s. While the trajectories are not repetitive, they all revolve around a center, indicating quasi-periodic dynamic behavior.

In Fig. 20a, b, the phase plane diagrams for the generator lateral vibrations at a rotational speed of 35 rad/s are depicted, showing chaotic behavior. The presence of nonrepetitive trajectories that are not random or unstable, but rather continuously changing paths around strange attractors, is observable. These features are indicative of chaotic behavior, supported by the presence of multiple

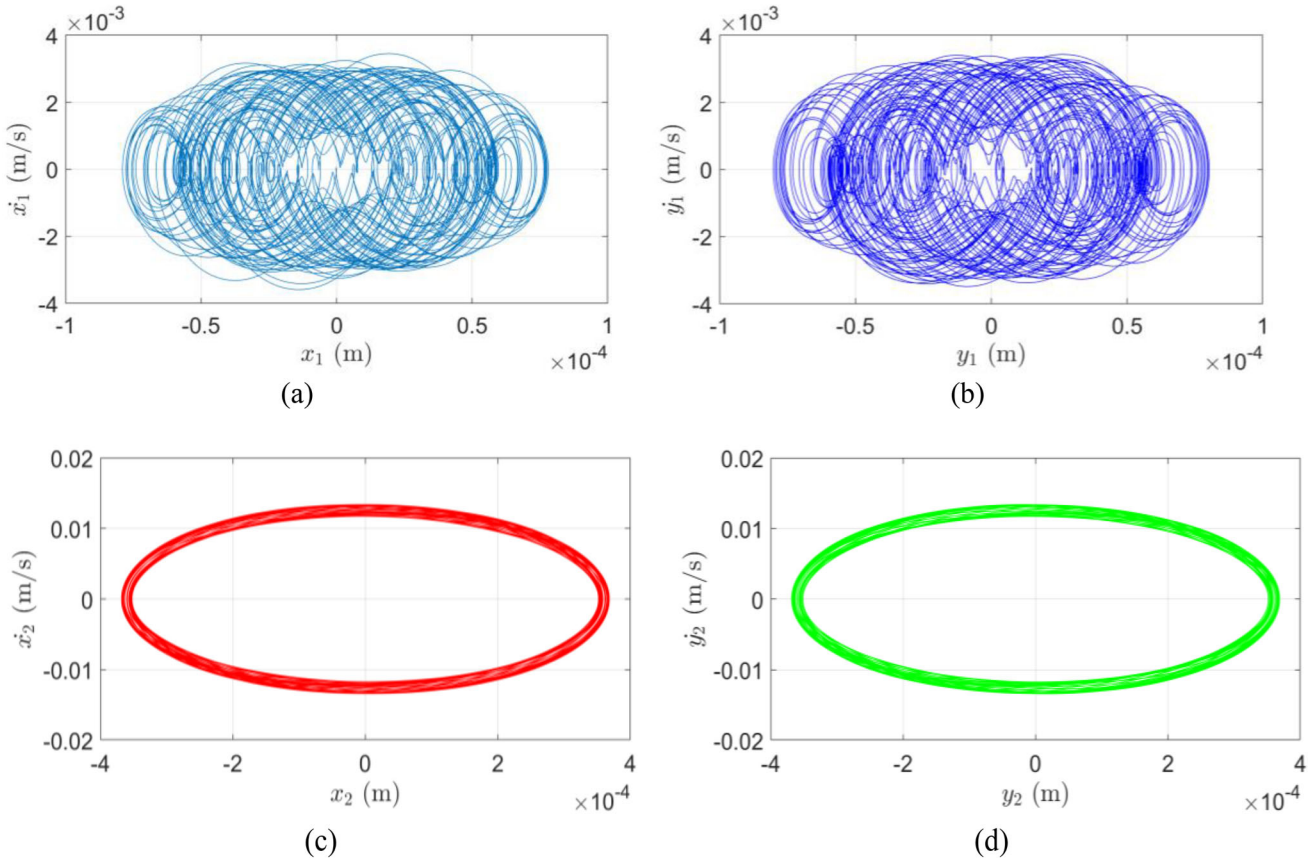

Fig. 20 Phase plane for the generator and hydrotourbine lateral vibrations at ω = 35 rad/s: **a** $\dot{x}_1$–x_1, **b** $\dot{y}_1$–y_1, **c** $\dot{x}_2$–x_2, **d** $\dot{y}_2$–y_2

frequencies in the frequency spectrum and the absence of periodicity in the corresponding time-domain plots. On the other hand, the phase plane diagrams for the hydroturbine lateral vibrations in Fig. 20c, d show that all trajectories rotate around a center, indicating harmonic dynamic behavior.

The phase plane diagrams for the latera vibrations of the generator and hydroturbine at a rotational speed of 45 rad/s are depicted in Fig. 21. In Fig. 21a, b, the phase plane is for the generator lateral vibrations, showing noncyclic trajectories around a center with a regular appearance. These trajectories are not random or unstable but exhibit quasiperiodic dynamic behavior. On the other hand, the phase plane for the hydroturbine lateral vibrations in Fig. 21c, d illustrates periodic behavior characterized by an increase in rotational speed and dominance of a single frequency. This dynamic behavior has emerged accordingly.

Poincare Section

In general, vibrational behaviors are classified into three categories: nonchaotic and harmonic behaviors, random behaviors, and chaotic behaviors. The Poincare section diagrams qualitatively represent these behaviors as follows:

1. For nonchaotic and harmonic behaviors, Poincare sections typically show the accumulation of one or a few points.
2. For random behaviors, Poincare sections display many points that are scattered irregularly.
3. For chaotic behaviors, Poincare sections exhibit an intermittent pattern between the previous two states, showing a large accumulation of points that have unique shapes and follow a specific order.

Each type of behavior is depicted qualitatively in the Poincare section.

Sometimes, analyzing images of strange attractors and their complex paths can be challenging. The phase space can be simplified via a method called the Poincare section or map. This approach corresponds to sampling the system whenever its trajectory intersects a cutting plane. It simplifies without altering the fundamental characteristics of the system. In Poincare diagrams, sampling is performed at a specific sampling rate from phase plane diagrams. This sampling rate is a relative to the rate of the system's rotational speed of the components.

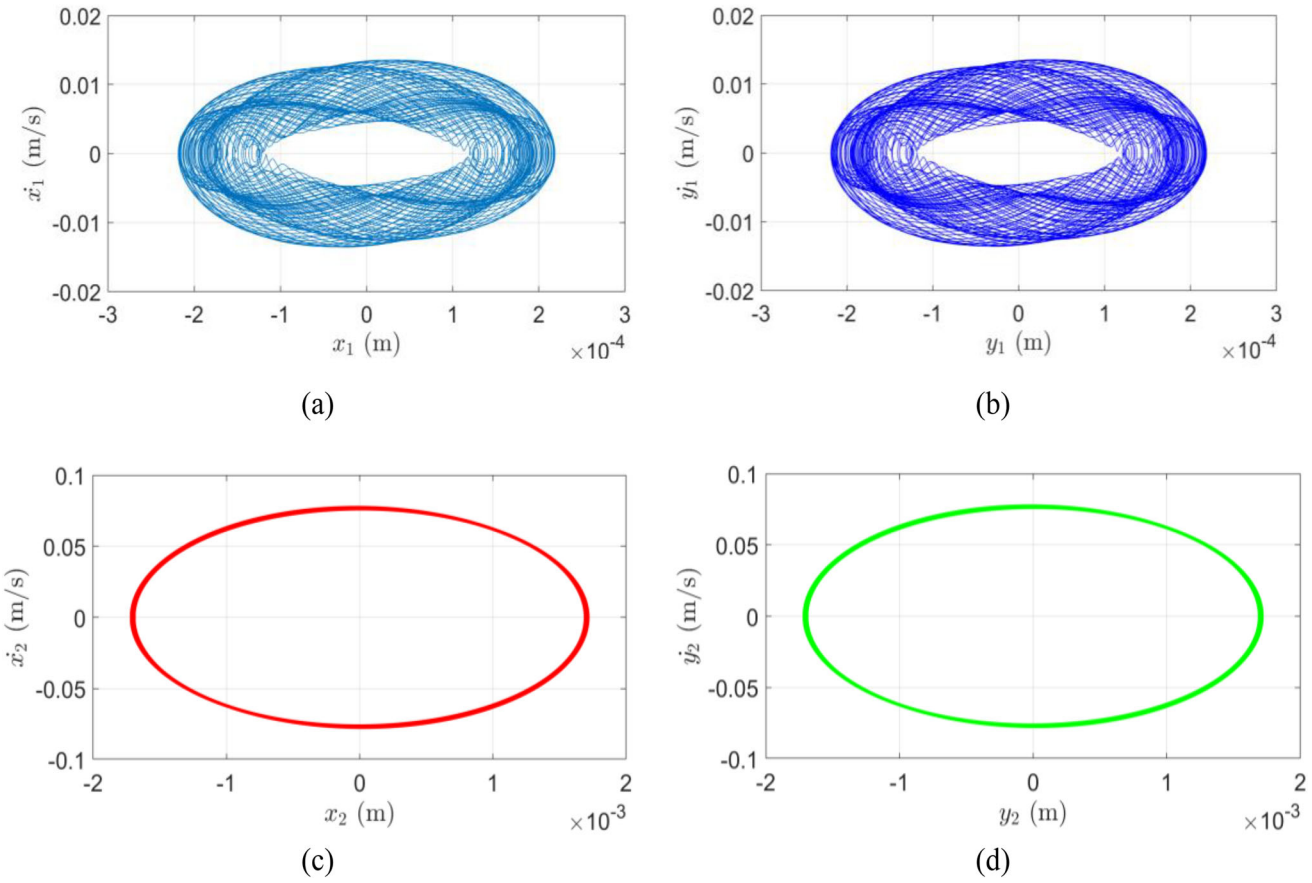

Fig. 21 Phase plane for the generator and hydrotourbine lateral vibrations at ω = 45 rad/s: **a** $\dot{x}_1$–x_1, **b** $\dot{y}_1$–y_1, **c** $\dot{x}_2$–x_2, **d** $\dot{y}_2$–y_2

In Fig. 22a, b, Poincare sections for the generator lateral vibrations at a rotational speed of 15 rad/s are shown. These figures display numerous points forming regular and different linear paths. In other words, the accumulation of these points within a range creates a regular pattern, confirming the presence of chaotic behavior due to their non-random and systematic distribution. Additionally, because the points are scattered in a disordered manner despite having similar and repetitive paths, a weaker chaotic behavior in the generator is suggested.

Figure 22c, d depict Poincare diagrams for the hydroturbine lateral vibrations at a rotational speed of 15 rad/s, where all the points are arranged in linear paths and rotate around a center. This indicates the presence of quasiperiodic behavior. Such dynamic behavior was also observed in the time-domain plots, frequency spectra, and phase plane diagrams of the hydroturbine.

Figure 23 depicts the Poincare sections for the lateral vibrations of the generator and hydroturbine at a rotational speed of 25 rad/s. In Fig. 23a, b, the Poincare section for the generator lateral vibrations shows numerous points forming quasi-circular paths around several strange attractors, continuously changing their trajectories. Despite their irregular appearance, they are stable and not random, which is indicative of chaotic behavior. In Fig. 23c, d, Poincare diagrams for the hydroturbine lateral vibrations are shown, where points form regular circular-shaped clusters around a center, rotating in a systematic manner. This type of movement and trajectory in the Poincare section of the hydroturbine indicates quasiperiodic behavior.

The Poincare diagrams for the lateral vibrations of the generator and hydroturbine at a rotational speed of 35 rad/s are depicted in Fig. 24. In Fig. 24a, b, the Poincare section for the generator lateral vibrations shows noticeable chaotic behavior. Many scattered points are visible, and despite their irregular appearance, they do not exhibit instability; instead, they form a regular pattern. Multiple consecutive ranges are observed, and all the points rotate in circular-like paths around these ranges.

Figure 24c, d illustrate the Poincare diagrams for the hydroturbine lateral vibrations, where all the points move in a semicircular ring with a specific order around a central point. This type of movement and path in the Poincare section of the hydroturbine indicate harmonic behavior.

In Fig. 25a, b, Poincare sections for the generator lateral vibrations at a rotational speed of 45 rad/s are depicted.

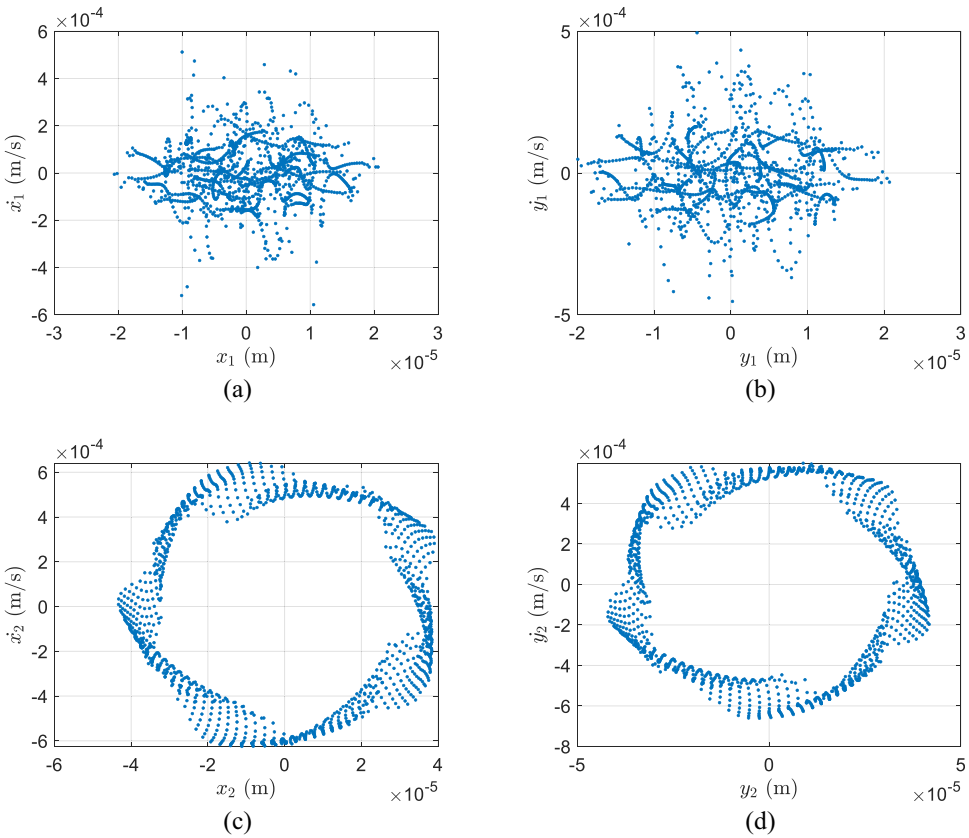

Fig. 22 Poincare sections of the generator and hydroturbine lateral vibrations at ω = 15 rad/s: **a** $\dot{x}_1$–x_1, **b** $\dot{y}_1$–y_1, **c** $\dot{x}_2$–x_2, **d** $\dot{y}_2$–y_2

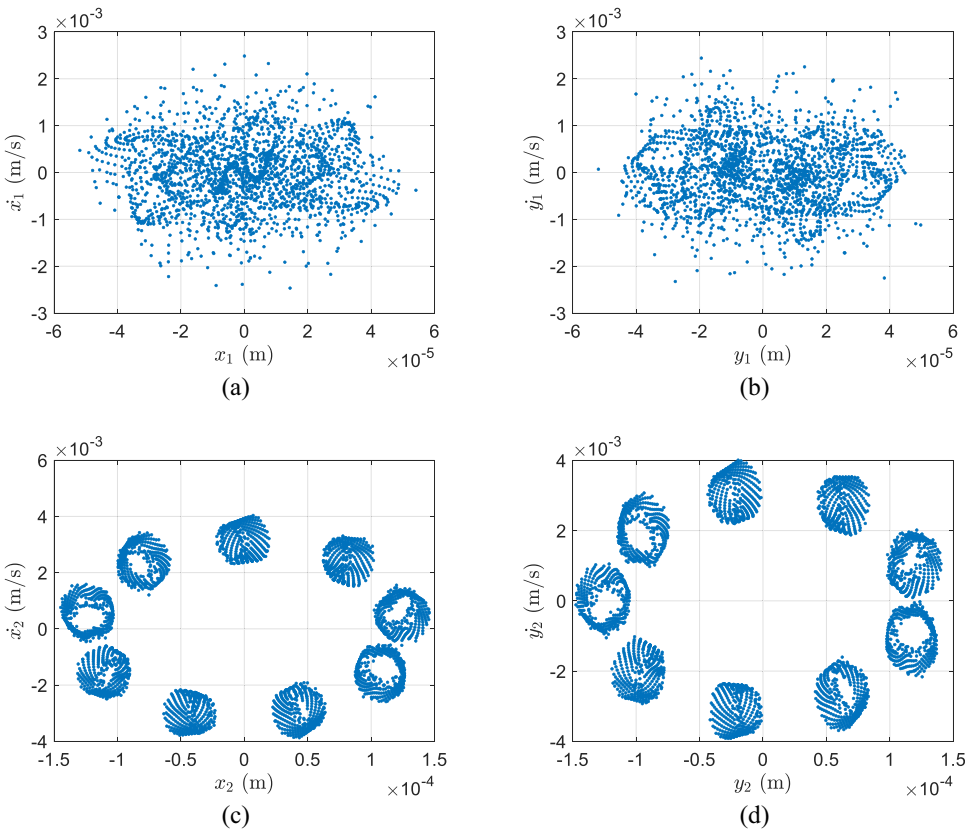

Fig. 23 Poincare sections of the generator and hydroturbine lateral vibrations at ω = 25 rad/s: **a** $\dot{x}_1$–x_1, **b** $\dot{y}_1$–y_1, **c** $\dot{x}_2$–x_2, **d** $\dot{y}_2$–y_2

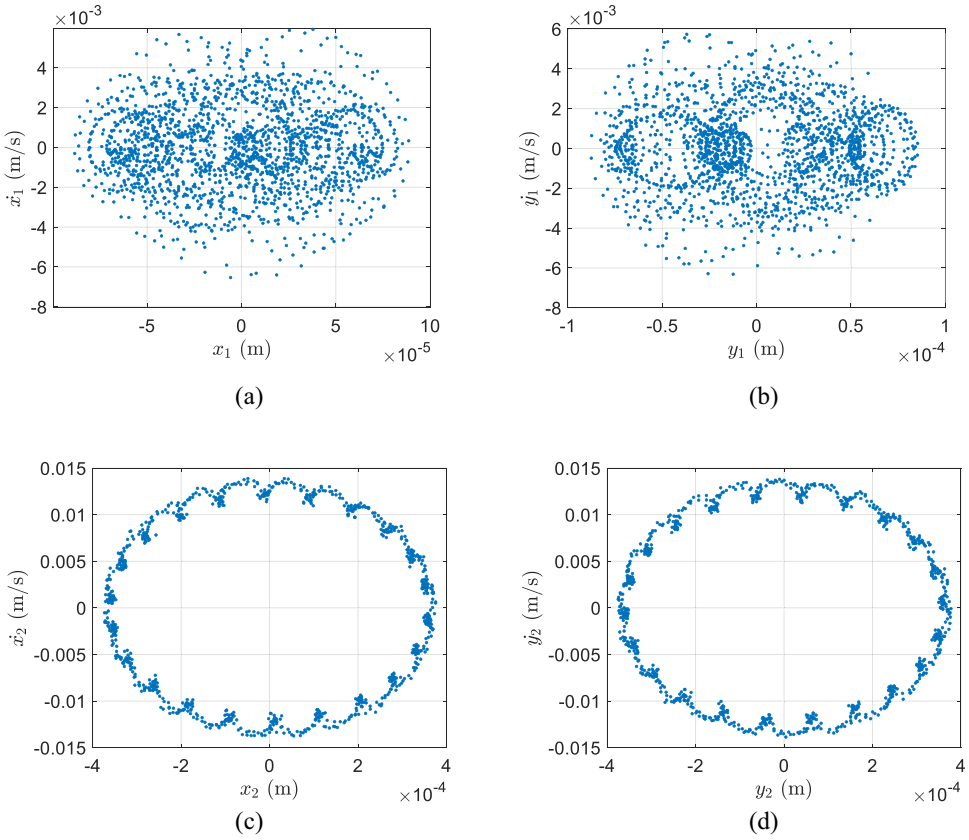

Fig. 24 Poincare sections of the generator and hydroturbine lateral vibrations at ω = 35 rad/s: **a** $\dot{x}_1$–x_1, **b** $\dot{y}_1$–y_1, **c** $\dot{x}_2$–x_2, **d** $\dot{y}_2$–y_2

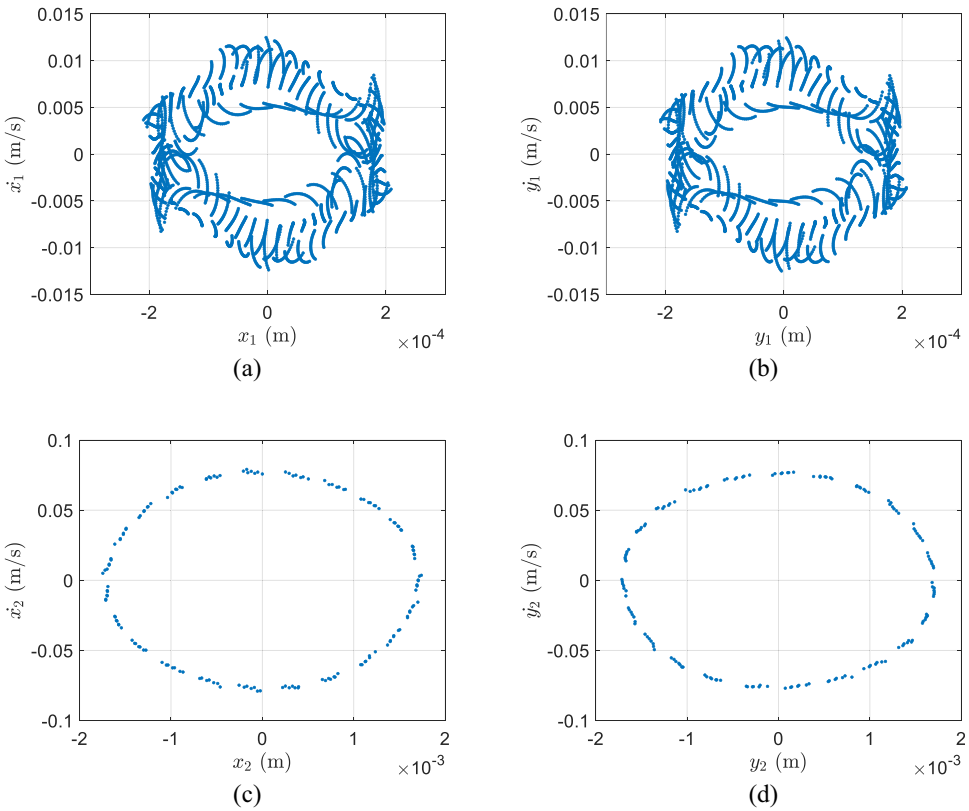

Fig. 25 Poincare sections of the generator and hydroturbine lateral vibrations at ω = 45 rad/s: **a** $\dot{x}_1$–x_1, **b** $\dot{y}_1$–y_1, **c** $\dot{x}_2$–x_2, **d** $\dot{y}_2$–y_2

The points form nonrepetitive clusters revolving around a center, yet they are not random or unstable; rather, they exhibit regularity. Therefore, the chaotic behavior identified in previous analyses is confirmed here as well. In Fig. 25c, d, Poincare diagrams for the hydroturbine lateral vibrations at a rotational speed of 45 rad/s are shown. The points form linear clusters in a regular circular or semicircular pattern. This type of point accumulation in the Poincare section indicates harmonic and quasiharmonic behavior.

In response to vibrating systems, various dynamic behaviors, such as periodic, quasiperiodic, and chaotic behaviors, generally occur. Chaotic dynamic behavior manifests as random and erratic responses outwardly, but fundamentally, these responses exhibit a well-defined dynamic. In the Poincare section diagrams of this article, numerous points are observed, but their behavior is not random; rather, the accumulation of these points forms a regular pattern. This phenomenon confirms the occurrence of chaotic behavior.

Conclusion

In this study, the modeling of the hydroturbine and generator was performed in a coupled manner. For the first time, the simultaneous impact of nonlinear forces of bearings, seals and rub-impact, as well as the gyroscopic effect, arcuate whirl and unbalanced magnetic pull on the lateral and torsional vibrations have been investigated. Governing equations were extracted by Lagrange method and numerical solutions were obtained by Runge–Kutta method. The vibration responses were obtained and plotted as time-domain graphs of the lateral and torsional vibrations. An analysis of these graphs indicates the presence of complex dynamic behaviors such as quasiperiodic and chaotic behaviors. For a more detailed analysis, frequency spectrum, phase plane and Poincare section were also plotted for the vibrations of the hydroturbine and generator at different rotational speeds.

It can be concluded that the presence of arcuate whirl and gyroscopic effect in the generator lead to complex dynamic behaviors such as quasiperiodic and chaotic behaviors. Similarly, the presence of mechanical seals reduces the amplitude of additional harmonics in the lateral vibrations of the hydroturbine. Furthermore, changes in the rotational speed significantly affect these behaviors, and increasing the rotational speed reduces the complexity of the machine's dynamic behavior.

This finding can be utilized to prevent chaotic occurrences in such systems. Moreover, these detailed analyses using vibration analysis will also be beneficial for fault diagnosis, and the presence of new frequencies will not lead to confusion. Considering the influence of geometric parameters such as the dimensions and distances of bearings and seals on the level of machine vibrations, this information can be used in the design and construction of these systems. Analyzing and studying dynamic behavior can assist in controlling machine vibrations under various conditions, thereby ensuring the production of high-quality and stable electricity. Preventing damaging vibrations helps avoid damage to both the generator and hydroturbine, thereby increasing machine efficiency in electricity generation operations and reducing downtime.

Chaotic vibrations are a type of dynamic motion that is not considered unstable, but owing to their irregularity and unpredictability, they are generally avoided. However, increasing the intensity of damaging vibrations can have detrimental effects on the system and potentially lead to instability. Given that damaging vibrations are harmful to the system, preventing their occurrence can also help avoid certain instabilities.

In this study, the dynamic modeling of the coupled hydroturbine-generator system is conducted, and the vibration response is determined by solving the governing equations using numerical methods. Specifically, the fourth-order Runge–Kutta method is implemented in MATLAB with Simulink to achieve precise simulations and analyses. Furthermore, the effects of various factors on the vibrations of hydroturbines and generators at different rotational speeds were analyzed and investigated. The result summary of this analysis are as follows:

1. With increasing rotational speed, the amplitude of lateral vibrations increases for both the generator and hydroturbine, but this increase does not occur at the same ratio for both.
2. In lateral-torsional vibrations, as the rotational speed increases, the complexity of the torsional vibrations θ decreases.
3. Coupled lateral-torsional vibrations show the influence of torsional vibrations on the lateral vibration axes at different rotational speeds.
4. Frequency spectrums of hydroturbine and generator vibrations reveal axis rotation frequencies and their harmonics, indicating nonlinear behavior.
5. Gyroscopic effects and arcuate whirl frequencies are observed in the generator frequency spectrum, varying with changes in rotational speed, demonstrating the dominant influence of various factors on the dynamic behavior of the hydroturbine and generator sets.
6. Multiple additional frequencies with a low amplitude are observed in the generator frequency spectrum, confirming the presence of chaotic behavior.
7. Harmonic and quasiharmonic dynamic behaviors are observed in hydroturbine vibrations, and mutual gyroscopic effects on the hydroturbine are observed at

certain speeds due to coupled hydroturbine and generator modeling, resulting in the creation of new combined frequencies with reduced amplitudes.

8. The amplitudes of some combined frequencies decrease due to the presence of mechanical seals, indicating that the mechanical seal influences the lateral vibrations of the hydroturbine.
9. The frequency spectrum of the hydroturbine indicate that the gyroscopic effect on the dynamic behavior decreases with increasing rotational speed. However, in generator lateral vibrations, quasi-periodic and chaotic behaviors occur.

Considering the approach of smart fault diagnosis in rotating machinery, the precise extraction of each system's features can be very useful in intelligent fault diagnosis methods. Therefore, in continuation, faults should also be included in the modeling of this system, and then, the features of the healthy and faulty systems should be extracted from the results and used as inputs for intelligent fault diagnosis methods. In general, vibration time signals, the frequency spectrum, the phase plane, and the Poincare section together confirm the existence of chaos in the system examined in this article.

Appendix

$$\begin{cases} K_{11} = \dfrac{A_1^2}{B^2}k_1 + \dfrac{(c+d)^2}{(b+c+d)^2}k_2 + \dfrac{d^2}{(b+c+d)^2}k_3 \\ K_{22} = \dfrac{A_2^2}{B^2}k_1 + \dfrac{b^2}{(b+c+d)^2}k_2 + \dfrac{(b+c)^2}{(b+c+d)^2}k_3 \\ K_{12} = \dfrac{-A_1A_2}{B^2}k_1 + \dfrac{b(c+d)}{(b+c+d)^2}k_2 + \dfrac{d(b+c)}{(b+c+d)^2}k_3 \end{cases} \tag{51}$$

$$\begin{cases} A_1 = (a+b)(b+c+d) \\ A_2 = ab \\ B = b(b+c+d) \end{cases} \tag{52}$$

$$\begin{cases} \Lambda_0 = \dfrac{\mu_0}{\delta_0}\dfrac{1}{\sqrt{1-\varepsilon^2}} \\ \Lambda_1 = \dfrac{2\mu_0}{\delta_0}\dfrac{1}{\sqrt{1-\varepsilon^2}}\left(\dfrac{1-\sqrt{1-\varepsilon^2}}{\varepsilon}\right) \\ \Lambda_2 = \dfrac{2\mu_0}{\delta_0}\dfrac{1}{\sqrt{1-\varepsilon^2}}\left(\dfrac{1-\sqrt{1-\varepsilon^2}}{\varepsilon}\right)^2 \\ \Lambda_3 = \dfrac{2\mu_0}{\delta_0}\dfrac{1}{\sqrt{1-\varepsilon^2}}\left(\dfrac{1-\sqrt{1-\varepsilon^2}}{\varepsilon}\right)^3 \end{cases} \tag{53}$$

$$\eta = \arctan\frac{y_2 + 2\dot{x}_2}{x_2 - 2\dot{y}_2} - \frac{\pi}{2}\operatorname{sgn}\left(\frac{y_2 + 2\dot{x}_2}{x_2 - 2\dot{y}_2}\right) - \frac{\pi}{2}\operatorname{sgn}(y_2 + 2\dot{x}_2) \tag{54}$$

$$G(x_2, y_2, \eta) = \frac{2}{\sqrt{(1 - x_2^2 - y_2^2)}}\left[\frac{\pi}{2} + \arctan\frac{y_2\cos\eta - x_2\sin\eta}{\sqrt{(1 - x_2^2 - y_2^2)}}\right] \tag{55}$$

$$V(x_2, y_2, \eta) = \frac{2 + (y_2\cos\eta - x_2\sin\eta)G(x_2, y_2, \eta)}{1 - x_2^2 - y_2^2} \tag{56}$$

$$S(x_2, y_2, \eta) = \frac{x_2\cos\eta + y_2\sin\eta}{1 - (x_2\cos\eta + y_2\sin\eta)^2} \tag{57}$$

Data availability The data that support the findings of this study are available from the corresponding author, upon reasonable request.

References

1. (2021) Hydropower special market Report. International Energy Agency
2. Awad H, Parrondo J (2024) Turbine inlet valve's self-excited vibrations risk the safe operation of hydropower plants. J Vib Eng Technol 12:3355–3371. https://doi.org/10.1007/s42417-023-01049-6
3. Dellinger N, François P, Lefebure D, Mose R, Garambois PA (2018) An experiment of a hydropower conversion system based on vortex-induced vibrations in a confined channel. Renew Energy 115:54–63. https://doi.org/10.1016/j.renene.2017.07.122
4. Xu B, Luo X, Egusquiza M, Ye W et al (2021) Nonlinear modal interaction analysis and vibration characteristics of a francis hydro-turbine generator unit. Renew Energy 168:854–864. https://doi.org/10.1016/j.renene.2020.12.083
5. Shen A, Chen Y, Zhou J et al (2021) Hydraulic vibration and possible exciting sources analysis in a hydropower system. Appl Sci 11:5529. https://doi.org/10.3390/app11125529
6. Xinjie L, Chaoshun L, Wencheng G et al (2019) Stability and dynamic characteristics of the nonlinear coupling system of hydropower station and power grid. Commun Nonlinear Sci Numer Simul 79:104919. https://doi.org/10.1016/j.cnsns.2019.104919
7. Perez-Loya JJ, Abrahamsson CJD, Lundin U (2018) Electromagnetic losses in synchronous machines during active compensation of unbalanced magnetic pull. IEEE Trans Ind Electron 66(1):124–131. https://doi.org/10.1109/tie.2018.2827991
8. Trivedi C (2017) A review on fluid structure interaction in hydraulic turbines: a focus on hydrodynamic damping. Eng Fail Anal 77:1–22. https://doi.org/10.1016/j.engfailanal.2017.02.021
9. Giannini O (2016) Unstable transient response of gyroscopic systems with stable eigenvalues. Mech Syst Signal Process 75:1–10. https://doi.org/10.1016/j.ymssp.2016.01.008
10. Zeng XH, Wu H, Lai J, Yu Y (2017) The effect of wheel set gyroscopic action on the hunting stability of high-speed trains. Veh Syst Dyn 55(6):924–944. https://doi.org/10.1080/00423114.2017.1293833
11. Ma H, Li H, Zhao X, Niu H, Wen B (2013) Effects of eccentric phase difference between two discs on oil-film instability in a

rotor–bearing system. Mech Syst Signal Process 41(1–2):526–545. https://doi.org/10.1016/j.ymssp.2013.05.006
12. Zhang LK, Ma ZY, Song BW (2013) Dynamic characteristics of a rub-impact rotor-bearing system for hydraulic generating set under unbalanced magnetic pull. Arch Appl Mech 83(6):17–830. https://doi.org/10.1007/s00419-012-0719-0
13. Patel TH, Zuo MJ, Zhao X (2012) Nonlinear lateral-torsional coupled motion of a rotor contacting a viscoelastically suspended stator. Nonlinear Dyn 69(1–2):325–339. https://doi.org/10.1007/s11071-011-0267-0
14. Li J, Chen D, Liu G, Gao X, Miao K, Li Y, Xu B (2019) Analysis of the gyroscopic effect on the hydro–turbine generator unit. Mech Syst Signal Process 132:138–152. https://doi.org/10.1016/j.ymssp.2019.06.020
15. Shi Y, Zhou J, Lai X, Xu Y, Guo W, Liu B (2021) Stability and sensitivity analysis of the bending-torsional coupled vibration with the arcuate whirl of hydro-turbine generator unit. Mech Syst Signal Process 149:107306. https://doi.org/10.1016/j.ymssp.2020.107306
16. Kong F, Song C, Zhuo Y (2023) Vibration fault analysis of hydropower units based on extreme learning machine optimized by improved sparrow search algorithm. J Vib Eng Technol 11:1609–1622. https://doi.org/10.1007/s42417-022-00660-3
17. Masalegoo SE, Soleimani A, Saeedi Masine H (2023) Experimental fault detection of rotating machinery through chaos-based tools of recurrence plot and recurrence quantitative analysis. Arch Appl Mech 93(3):1259–1272. https://doi.org/10.1007/s00419-022-02326-8
18. Soleimani A, Khadem SE (2015) Early fault detection of rotating machinery through chaotic vibration feature extraction of experimental data sets. Chaos Solitons Fractals 78:61–75. https://doi.org/10.1016/j.chaos.2015.06.018
19. Feng J, Men Y, Zhu G, Li Y, Luo X (2022) Cavitation detection in a Kaplan turbine based on multifractal detrended fluctuation analysis of vibration signals. Ocean Eng 263:112232. https://doi.org/10.1016/j.oceaneng.2022.112232
20. Xu BB, Chen DY, Zhang H, Li C, Zhou J (2018) Shaft misalignment induced vibration of a hydraulic turbine generating system considering parametric uncertainties. J Sound Vib 435:74–90. https://doi.org/10.1016/j.jsv.2018.08.008
21. Song Z, Liu Y, Guo P, Feng J (2018) Torsional vibration analysis of hydro-generator set considered electromagnetic and hydraulic vibration resources coupling. Int J Precis Eng Manuf 19(7):939–945. https://doi.org/10.1007/s12541-018-0111-2
22. Xu BB, Chen DY, Zhang H, Zhou R (2015) Dynamic analysis and modeling of a novel fractional-order hydro-turbine-generator unit. Nonlinear Dyn 81:1263–1274. https://doi.org/10.1007/s11071-015-2066-5
23. Shi Y, Zhou J (2022) Stability and sensitivity analyses and multi-objective optimization control of the hydro-turbine generator unit. Nonlinear Dyn 107:2245–2273. https://doi.org/10.1007/s11071-021-07009-7
24. Zhuang K, Huang S, Fu X, Chen L (2022) Nonlinear hydraulic vibration modeling and dynamic analysis of hydro-turbine generator unit with multiple faults. Energies 15(9):3386. https://doi.org/10.3390/en15093386
25. Sun W, Guo Z (2021) Mathematical modeling and nonlinear vibration analysis of a coupled hydro-generator shaft-foundation system. Commun Nonlinear Sci Numer Simul 98:105776. https://doi.org/10.1016/j.cnsns.2021.105776
26. Li Z, Liu F, Cai G et al (2024) Method of non-stationary random vibration reliability of hydro-turbine generator unit. Acta Mech 40:523427. https://doi.org/10.1007/s10409-024-23427-x
27. Wang W, Shang Y, Yao Z (2022) A predictive analysis method of shafting vibration for the hydraulic-turbine generator unit. Water 14:2714. https://doi.org/10.3390/w14172714
28. Zhuang K, Huang S, Fu X, Chen L (2022) Nonlinear hydraulic vibration modeling and dynamic analysis of hydro-turbine generator unit with multiple faults. Energies 15:3386. https://doi.org/10.3390/en15093386
29. Wu W, Pang J, Liu X, Zhao W, Lu Z, Yan D, Zhou L, Wang Z (2023) Effect of unbalanced magnetic pull of generator rotor on the dynamic characteristics of a pump-turbine rotor system. Water 15:1120. https://doi.org/10.3390/w15061120
30. Ishibashi T, Kawai T (2019) Modelling of oil film bearings. In: Proceedings of the 2nd Japanese Modelica Conference, vol 148, pp 115–121. https://doi.org/10.3384/ecp18148115
31. Adiletta G, Guido AR, Rossi C (1996) Chaotic motions of a rigid rotor in short journal bearings. Nonlinear Dyn 10:251–269. https://doi.org/10.1007/BF00045106